RSC Advances

PAPER

View Article Online
View Journal | View Issue

Cite this: *RSC Adv.*, 2025, **15**, 29836

Multiscale analysis of Rb_2NaInI_6: from electronic structure to device performance for next-generation perovskite solar cells

Akram Hossan Mahedi,[ab] Salah Uddin,[ab] Mohammad Yasin Hayat Khan,[ab] Md. Tarekuzzaman,[ab] O. Alsalmi,[c] Md. Rasheduzzaman,[ab] S. M. G. Mostafa,[b] M. Moazzam Hossen[d] and Md. Zahid Hasan*[ab]

The harmful effects and long-term unpredictability of conventional compounds made from lead have driven a more intense quest for practical, stable, and ecologically acceptable lead-free perovskite components. Among the exciting prospects, the pair of perovskites Rb_2NaInI_6 stands out for its special structural, electrical, and optical properties, therefore offering a possible subsequent-generation light-absorbing substance for photovoltaic energy and optoelectronic use. We study Rb_2NaInI_6 holistically in this work, utilizing a mixed computational method. The density functional theory (DFT) computations using WIEN2k verify their cubic $Fm\bar{3}m$ organization with an optimal lattice consistency of 12.25 Å, guaranteeing strong structural integrity. Whereas its density of states (DOS) assessment shows substantial hybridization concerning In-5s and I-5p orbitals, boosting charge transport, the semiconductor band structure provides a secondary bandgap of 0.68 eV. Strong absorption in the visible to light spectrum, with a significant coefficient of attraction and low reflectance (<30%), makes optical analysis very appropriate for solar power plants and optoelectronic device uses. Furthermore, its dielectric material functions alongside refractive index, pointing to great possible usage in photonic devices and wavelength guides. Using SCAPS-1D, we simulate four straight heterojunction topologies, including various electron transport layers (ETLs), ZnO, WS_2, WO_3, and PCBM, *via* Pt as the rear contact as well as CBTS as the hole transport layer, thereby exploring its device-level efficiency. Under AM 1.5G enlightenment the FTO/ZnO/Rb_2NaInI_6/CBTS/Pt arrangement obtained the best leads to between these with an open-circuit voltage (V_{oc}) of 1.39 V, short-circuit current density (J_{sc}) at 21.39 mA cm^{-2}, fill factor (FF) of 89.83%, particularly a staggering power conversion efficiency (PCE) of 26.84%. When combined with ideal ETLs, Rb_2NaInI_6 expresses a lucky, lead-free perovskite-absorbing material that opens routes for developing stable, effective, and ecologically conscious solar panels made of perovskite. This work highlights the need to accelerate development and enhance new solar components by merging first-principles modelling with device training exercises.

Received 3rd July 2025
Accepted 14th August 2025

DOI: 10.1039/d5ra04739k

rsc.li/rsc-advances

1. Introduction

Advancing innovative materials is crucial for progress in research and technology across various sectors, including energy, electronics, healthcare, and the environment. However, traditional experimental methods for discovering and optimizing materials are slow, costly, and labor-intensive—often taking over two decades to move from concept to commercialization.[1] This sluggish tempo engenders a bottleneck in advancement in technology, highlighting the pressing necessity for expedited and more efficient approaches to material discovery. In response to these challenges, computational materials science has emerged as a groundbreaking discipline, enabling researchers to predict material properties and design innovative molecules with unprecedented speed and accuracy. Computational technologies diminish dependence on experimentation and failure methods of testing and substantially decrease scientific and development expenditures. Research by Allison *et al.* indicates that utilizing computational design can decrease time to market and yield a return on your investment of 300% to 700%.[2] Density Functional Theory (DFT) has emerged as one of the many potent and adaptable computing approaches. Rooted in the concept of quantum mechanics, DFT

[a]*Materials Research and Simulation Lab, Department of Electrical and Electronic Engineering, International Islamic University Chittagong, Kumira, Chittagong, 4318, Bangladesh. E-mail: zahidhasan.02@gmail.com*

[b]*Department of Electrical and Electronic Engineering, International Islamic University Chittagong, Kumira, Chittagong, 4318, Bangladesh*

[c]*Department of Physics, College of Science, Umm Al-Qura University, Makkah 21955, Saudi Arabia*

[d]*Department of Computer Science and Engineering, International Islamic University Chittagong, Kumira, Chittagong, 4318, Bangladesh*

provides a first-principles framework for examining the electronic makeup of molecules, atoms, and compressed material systems.[1,3–5] The complicated many-body Schrödinger equation does not need to be solved directly since DFT makes it possible to calculate ground-state parameters based just on electron density. This renders it highly beneficial across several research domains, encompassing molecular morphologies,[6,7] elements and interfaces,[8] flaws in solids,[9–11] as well as the examination of electrical transport,[12,13] optical characteristics,[14] and contributing behavior.[15] The accuracy of DFT is contingent upon the exchange–correlation functional utilized, which presents difficulties in accurately simulating specific interactions; nonetheless, ongoing advancements and novel approximations have markedly improved its predictive efficacy. Consequently, DFT has become essential in contemporary materials science, connecting theoretical predictions with experimental confirmations. This paper introduces an innovative approach that combines DFT with the solar panel Cell. The term capacitor Simulators (SCAPS-1D) to examine the optoelectronic characteristics and performance of the Rb_2NaInI_6 double perovskite, a potential contender for solar power applications. We seek to deliver an extensive comprehension of the material characteristics and photovoltaic performance of this free from lead double perovskite by integrating atomistic simulations with device-level modeling.[16,17] After identifying viable materials, a crucial stage is the filtration and selection process. Preliminary screening often emphasizes the exclusion of materials containing hazardous substances such as lead (Pb) and mercury (Hg), as well as those that incorporate rare and costly elements like palladium (Pd) and platinum (Pt).[18–20] Advanced Training filtering processes, based on computational projections of properties such as formation electrical power, bandgap, along with thermodynamic rigidity (*e.g.*, hull energy), enhance the refinement of candidate materials, guaranteeing that only the best potential candidates are given preference for exploratory synthesis and testing.[21–23] Perovskites have transformed the domain of photovoltaics in the last decade, mostly due to their beneficial material characteristics and straightforward production. These materials generally possess a crystalline structure defined by the formula ABX_3, in which 'A' represents a monovalent cation, 'B' denotes a divalent metal cation, and 'X' signifies a halide anion.[24–26] They are renowned for their ideal direct bandgaps, robust absorption of visible light, minimal effective carrier masses, and outstanding charge transport properties, including extended diffusion lengths, lifetimes, and elevated mobilities. Furthermore, their inherent defect tolerance and multifunctionality broaden their applicability beyond photovoltaics to encompass photocatalysis, light-emitting diodes (LEDs), unpredictable optical devices, photodetectors, scintillators, memristors, and field-effect transistors.[27–29] Since the initial demonstration of a perovskite solar cell (PSC) in 2009, which exhibited a power conversion efficiency (PCE) of 3.8%, efficiencies have escalated to over 25.8% by 2022. Notwithstanding these notable accomplishments, the actual implementation of PSCs is impeded by two critical concerns: the environmental and health risks linked to lead-based perovskites and their inherent instability under operational settings.[30,31] Strategies to boost stability have involved substituting organic cations with inorganic counterparts such as Cs^+ and Rb^+, which fortify lattice connections and improve heat and moisture stability.[32–34] Nonetheless, the issue of lead toxicity persists, prompting significant investigation into lead-free alternatives. Lead-free perovskites, specifically those composed of tin (Sn^{2+}) and germanium (Ge^{2+}), have surfaced as appealing alternatives owing to their analogous electrical structures and optoelectronic characteristics. Regrettably, these materials exhibit inadequate ambient stability, as Sn^{2+} and Ge^{2+} are susceptible to oxidation into their tetravalent states (Sn^{4+} and Ge^{4+}), leading to fast deterioration of device performance.[35,36] An alternate method is hetero valent replacement, in which two Pb^{2+} ions are substituted by a mixture of monovalent (+1) and trivalent (+3) cations, resulting in lead-free double perovskites (LFDPs) *via* the following formula: $A_2B(I)B(III)X_6$.[37–39] These compounds provide enhanced chemical maneuverability and customization of band structure and optical characteristics, expanding the possibilities for material design. The structural paradigm of double perovskites originated in the early 20th century, with K_2NaAlF_6 recognized as one of the initial documented instances.[38–41] Recent studies have concentrated on inorganic LFDPs employing Cs^+ or Rb^+ at the A-site, as these cations strengthen the contact between cations and $[BX_6]^-$ octahedra, leading to improved structural integrity.[34,42] Sn-based perovskites have commendable photovoltaic properties, featuring band gaps ranging from 1.2 to 1.4 eV—approaching the Shockley–Queisser optimum bandgap of 1.34 eV[43–45] and power conversion efficiencies above 13% in certain studies.[46,47] Oxidation difficulties continue to exist, driving the persistent quest for innovative LFDPs that integrate stability, ideal bandgaps, and enhanced electrical characteristics. Elpasolites, a category of low-dimensional functional materials characterized by the general formula $A_2M(I)M(III)X_6$, include more than 350 recognized structures.[48,49] Building upon the research of Z. Zhang *et al.*, who achieved a power conversion efficiency of 6.37% with a hydrogenated Rb_2NaInI_6 structure, our investigation advances this field by employing sophisticated computational methods to enhance and model device performance. We utilized an inverted (p-i-n) perovskite solar cell architecture, maintaining ZnO as the electron transport layer (ETL) and Cu_2BaSnS_4 (CBTS) as the hole transport layer (HTL). Simulations were performed under AM 1.5G illumination with SCAPS-1D (version 3.8), enabling the optimization of essential parameters like absorber layer thickness, loading concentration, and defect density. Furthermore, we methodically examined the influence of HTL thickness and doping concentrations on device efficacy. To enhance comprehension of the interfacial characteristics and band alignment, we simulated devices employing four distinct electron transport layers: ZnO, WS_2, WO_3, and [6,6]-phenyl-C_{61}-butyric acid methyl ester (PCBM). ZnO and WS_2 exhibit elevated electron mobility and advantageous energy-level alignment with perovskite absorbers, whilst WO_3 and PCBM provide adjustable electronic characteristics and compatibility with scalable processing methods.[50–54] Our simulations demonstrated remarkable maximum power conversion efficiencies of 26.84% (ZnO), 26.61% (WS_2), 26.73%

(WO_3), and 26.26% (PCBM), underscoring the significant potential of hydrogenated Rb_2NaInI_6 in inverted perovskite solar cell topologies. Experimental power conversion efficiencies (PCEs) for analogous materials like $Cs_2AgBiBr_6$ are modest, varying from 1.66%[52] to 21.88%[55] in optimized setups, although theoretical and computational analyses persist in highlighting their promise for high-performance solar applications.[56–58] DFT studies of essential electronic properties—namely band structure, bandgap, density of states (DOS), and electron density mapping—provide critical insights into the applicability of halide perovskites for optoelectronic applications.[59–61] Our research constitutes the inaugural comprehensive endeavor to amalgamate DFT and SCAPS-1D simulations for the assessment of the photoelectric potential of the Rb_2NaInI_6 double perovskite. By integrating atomistic insights with device-level performance modeling, we offer a comprehensive understanding of this material's appropriateness for subsequent-generation, without lead, perovskite solar cells. This study establishes a foundation for subsequent experimental validations and informs the conceptualization of trustworthy, high-efficiency LFDP-based solar energy sources.

2. Materials and methodology

2.1. First-principles computations of Rb_2NaInI_6 absorber utilizing DFT

This work investigates the characteristics of the substances using density functional theory (DFT) and WIEN2k software under the FP-LAPW approach.[62–64] Three primary phases define the computational process: structure optimization and optoelectronic property computation. The Generalized Gradient Approximation (GGA) method—more especially, the Perdew–Burke–Ernzerhof (PBE)[65] exchange–correlation function—is used for the optimization of structural elements.[66] Keeping all of the energy regarding the foundational set size ($R \times K_{max} = 8$) and k-point grid (13×13) guarantees convergence. We consider a 10^{-6} Ry total energy convergence threshold. Using TB-mBJ potential, which is known for its accuracy in band gap prediction, optoelectronic features are investigated.[67] The relaxation interval approximated performance (RTA = 10^{-14} s) helps one to find semi-classical transportation coefficients. Moreover, the thermodynamic durability of the materials[68] is verified by computing the phonon band arrangement and density of states (DOS) employing the WIEN2k algorithm with the limited displacement approach. Employing the Kramers–Kronig relations, one finds optical parameters, including the absorption coefficients, reflectance, conductivity of electric current, refractive index, energy loss function, and the actual portion of the dielectric property function from the imaginary component of the dielectric property function. The mathematical equations for computing these optical characteristics are presented below; each symbol has a usual interpretation.[69,70]

2.2. Numerical simulation employing SCAPS-1D

Comprehending the utility and efficiency of solar energy cells depends on using mathematical models like SCAPS-1D. Through numerical solution of equations such as a single-dimensional Poisson's equation, scientists can obtain an important understanding of the relationship between charge distribution inside a material made of semiconductors and its electrostatic potential. Poisson's equation provides a useful illustration of eqn (1).[71–73] The above equation explains in any particular semiconductor material the link between the charge transportation and the electromagnetic potential. Utilizing numerical solutions, scientists may examine and forecast the effect of different elements on solar cell operation. This analytical method clarifies the main aspects influencing the energy efficiency of sunlight-sensitive cells through significant elements.[74]

$$\frac{\partial}{\partial x}\left(\varepsilon(x)\frac{\mathrm{d}\psi}{\mathrm{d}x}\right) = q[p(x) - n(x) + N_{D^+}(x) - N_{A^-}(x) + \mathrm{pt}(x) - nt(x)] \quad (1)$$

In this instance, ε_0 signifies the permittivity of free space, ψ denotes the potential of electricity, and ε_r indicates the proportional permittivity. The symbols ND as well as NA refer to the adjustment of charged donors as well as acceptors, while n among p indicate the densities of electrons plus holes. P_n also ρ_p show that the distributions of electrons and holes, respectively, and q represents the electric charge. Considering all processes simultaneously-recombination, generation, drift, and diffusion—the continuity equation emerges as the primary equation of importance. Eqn (2) and (3), which are continuity equations, describe the changes in the counts of electrons and holes, respectively, taking into account the various mechanisms at play.

$$\frac{1}{j}\frac{\mathrm{d}J_p}{\mathrm{d}x} + R_p(x) - G_p(x) = 0 \quad (2)$$

$$-\frac{1}{j}\frac{\mathrm{d}J_n}{\mathrm{d}x} + R_n(x) - G_n(x) = 0 \quad (3)$$

Under this situation, J_n and J_p correspondingly reflect the current density of holes as well as electrons. R_n and R_p show the relative recombination rates; G_n and G_p show the hole in addition to the electron generation rates. Eqn (4) and (5) help one to determine the current densities of electrons and holes in solar cells utilizing the charged carrier drift-diffusion mathematical equations. The following formulas clarify the way holes as well as electrons migrate across the dielectric material in response to changing electromagnetic fields, concentration shifts, carrier production, and recombination events.

$$J_n = q\mu_n n\varepsilon + qD_n\partial n \quad (4)$$

$$J_p = q\mu_p n\varepsilon + qD_p\partial p \quad (5)$$

In this context, D_n and D_p demonstrate these diffusion coefficients, whereas μ_n and μ_p correspondingly reflect the mobility of electrons and holes. Carrier lifetime and mobility, which are represented by the Albert Einstein relation, significantly affect their diffusion coefficient of friction. Furthermore, the

absorbance constant of sheets was determined using a modified form of the old sqrt ($h\nu - E_g$) model based on the recently updated E_g-sqrt structure. Eqn (6) therefore shows this coupled with using the "Torque laws", which offer understanding of substance absorption behavior depending upon their band gap energy.

In the provided context, the symbols $h\nu$ represent the photon energy, and E_g represents the band gap and absorption coefficient of the material. Eqn (7) and (8) demonstrate the relationship between the model constants α_0 and β_0 with the traditional model constants A and B. This relationship allows for a clear understanding of how these parameters are interconnected and how they relate to the material's optical properties.

$$\alpha_0 = A\sqrt{E_g} \tag{6}$$

$$\beta_0 = \frac{B}{\sqrt{E_g}} \tag{7}$$

Fig. 1, therefore, displays our performance in the SCAPS-1D modeling. First, we created a model of our solar cell using the program. This involved organizing all the several layers, including ETLs, and that Rb_2NaInI_6 material we employ as an electromagnetic absorber—the perovskite component. By simulating several varying situations to obtain the J–V curves. We varied the voltage, light intensity (AM 1.5G), and temperature while inputting key material properties like bandgap, electron affinity, and carrier mobility. The simulation results, including J–V curves, capacitance, QE, and Mott–Schottky plots, were matched with experimental data. The software internally solves drift-diffusion, Poisson, and continuity equations to model electron behavior. Finally, we visualized and analyzed the data to assess solar cell performance.

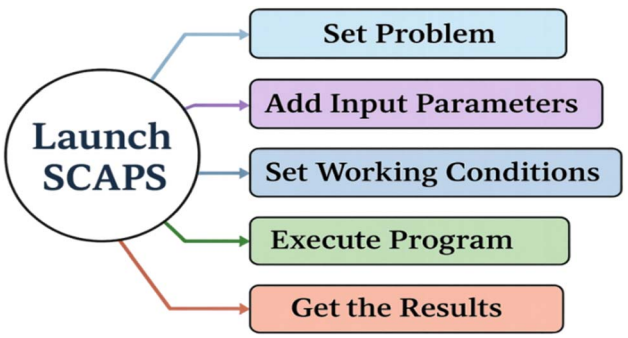

Fig. 1 The operational methodology of SCAPS-1D.

2.3. Structure of the device

Fig. 2a illustrates the stratified architecture of a perovskite solar cell (PSC) including Rb_2NaInI_6 as the light-absorbing layer. The design commences with a fluorine-doped tin oxide (FTO) film at the base, functioning as a translucent conducting electrode that permits sunlight to penetrate the cell. The Electron Transportation Layer (ETL) is positioned beneath the FTO, comprised of one of four substances: ZnO,[75] WS_2,[75] WO_3,[76] or PCBM,[75] enabling electron transfer from the absorbers to the FTO. The absorbing layer, composed of Rb_2NaInI_6, captures sunlight and produces a pair of electron–holes. Furthermore, the Hole Transport Layer (HTL), consisting of CBTS,[75] facilitates the transfer of holes to the upper electrode. The rear contact, composed of Platinum (Pt), finalizes the cell by collecting holes and enabling their mobility, thereby generating an ongoing current flow while subjected to sunlight.

Fig. 2b illustrates that the photoelectric device architecture incorporates Rb_2NaInI_6 as the primary absorber layer, complemented by meticulously positioned holes as well as electron transport layers ETLs along with HTL to facilitate effective separation of charged particles and collection. The heterogeneous structures comprise FTO, an electron transport layer (ETL) such as ZnO, WS_2, WO_3, or intentionally PCBM, Rb_2NaInI_6, CBTS, and additionally Pt, with each layer selected to enhance energy alignment. The ETLs and Rb_2NaInI_6 exhibit

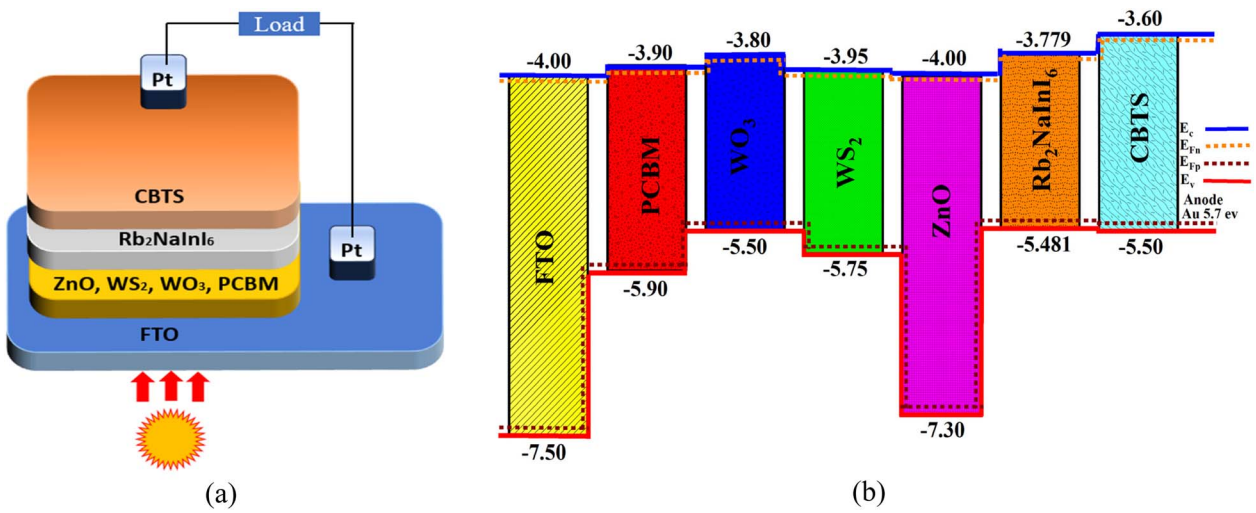

Fig. 2 (a) Device architecture based on Rb_2NaInI_6, (b) energy band alignment between FTO/ETLs/Rb_2NaInI_6/CBTS/Pt.

Table 1 The input settings for FTO, ETLs, HTL, as well as an absorber layer

Parameter	FTO[77]	WS_2 (ref. 59)	WO_3 (ref. 78)	ZnO[59]	PCBM[59]	CBTS[59]	Rb_2NaInI_6
Thickness (nm)	500	100	50	50	50	100	1000
Bandgap (E_g) (eV)	3.5	1.8	2	3.3	2	1.9	1.702
Electron affinity (χ) (eV)	4	3.95	3.8	4	3.9	3.6	3.779
Dielectric permittivity (ε_r)	9	13.6	4.8	9	3.9	5.4	5.06
Effective DOS (conduction) (cm^{-3})	2.2×10^{18}	1.0×10^{18}	2.2×10^{21}	3.7×10^{18}	2.5×10^{21}	2.2×10^{18}	3.053×10^{16}
Effective DOS (valence) (cm^{-3})	1.8×10^{19}	2.4×10^{19}	2.2×10^{21}	1.8×10^{19}	2.5×10^{21}	1.8×10^{19}	9.945×10^{17}
Electron thermal velocity (cm s^{-1})	1.0×10^{7}	1.0×10^{7}	1.0×10^{7}	1.0×10^{7}	1.0×10^{7}	1.0×10^{7}	1.0×10^{7}
Hole thermal velocity (cm s^{-1})	1.0×10^{7}	1.0×10^{7}	1.0×10^{7}	1.0×10^{7}	1.0×10^{7}	1.0×10^{7}	1.0×10^{7}
Electron mobility (cm^2 V^{-1} s^{-1})	20	100	30	100	0.2	30	155.6
Hole mobility (cm^2 V^{-1} s^{-1})	10	100	30	25	0.2	10	15.25
Donor density (ND) (cm^{-3})	1×10^{18}	1×10^{18}	6.35×10^{17}	1×10^{18}	0	0	0
Acceptor density (NA) (cm^{-3})	0	0	0	0	2.93×10^{17}	1×10^{18}	1×10^{15}
Defect density (Nt) (cm^{-3})	1×10^{15}	1×10^{15}	1×10^{15}	1×10^{15}	1×10^{15}	1×10^{15}	1×10^{15}

compatible band alignments, leading to the quasi-Fermi levels representing electrons (E_{fn}) along with holes (E_{fp}) aligning with the conduction band (E_C) and valence band (E_V) edges, for example, facilitating efficient electron and hole transportation to their corresponding electrodes. The HTL CBTS is deliberately designed to promote hole transport to the Pt back contact while reducing recombination losses. The resulting device architecture utilizes work function differences, employing FTO as the front contact (4.0 eV) along with Pt as the rear contact (5.7 eV), thereby inducing electron transportation toward the FTO and hole migration toward the Pt, which improves charge collection. Among the ETLs, WS_2,[75] WO_3,[76] or PCBM[75] exhibit their conduction band edges that are closely aligned with Rb_2NaInI_6, facilitating efficient electron transport and reducing energy loss. Although ZnO[75] has a lower conduction band minimum, it may create energy barriers that affect carrier dynamics. The HTL CBTS is compatible with Rb_2NaInI_6, facilitating efficient hole extraction. The band alignment underlies the observed solar performance, with ZnO and WO_3 achieving better efficiencies due to advantageous energy level alignment. Table 1 outlines key parameters such as thickness, bandgap, electron affinity, dielectric constant, effective density of states (VB and CB), carrier mobilities, shallow acceptor/donor densities, and defect density (N_t). These values were carefully chosen based on fabrication data from peer-reviewed literature to ensure accurate simulation results.

In the simulations, parameters such as electron and hole thermal velocities (set at 10^7 cm s^{-1}) were standardized across all layers. Interface defect layers (IDLs) were introduced between the ETL/Rb_2NaInI_6 and Rb_2NaInI_6/HTL interfaces to better reflect real conditions, as detailed in Table 2. Fluorine-doped tin oxide (FTO) served as the transparent, conductive anode, while platinum (Pt) was used as the cathode for its suitable work function. Simulations were conducted under standard AM 1.5G illumination at 1000 W m^{-2} and 300 K. Only defect-related recombination was considered, excluding radiative and Auger processes. The voltage range was set from 0 to 1.8 V to capture the full operational window.

3. Results and discussion

3.1. Structural properties and stability of Rb_2NaInI_6

The structural properties of Rb_2NaInI_6 reveal that it crystallizes in a cubic double-perovskite-type system, adopting the $Fm\bar{3}m$ (space group 225) symmetry.[76] The optimized atomic arrangement within the unit cell places Rb atoms at the 8c (0.25, 0.25, 0.75) positions, Na at 4b (0.5, 0, 0), In at 4a (0, 0, 0), and I at 24e (0.2415, 0, 0). This well-ordered atomic configuration contributes to the stability and symmetry of the crystal structure. Upon structural optimization, the calculated lattice parameter was found to be $a = b = c = 12.19$ Å, leading to a unit cell volume of 1810.05 $Å^3$. Such a lattice framework indicates a spacious and stable arrangement of cations and anions, reinforcing the perovskite-derived nature of the compound. The three-dimensional visualization of the optimized crystal structure as illustrated in Fig. 3 further confirms the uniformity and connectivity of the octahedral framework, where NaI_6 and InI_6 octahedra share corners, maintaining a stable coordination

Table 2 Interface characteristics employed for this perovskite solar panel

Interface	ETL/absorber[59]	Absorber/HTL[59]
Defect type	Neutral	Neutral
Electron cross-section measurement (cm^2)	1×10^{-17}	1×10^{-18}
Acquire cross-sectional data for apertures (cm^2)	1×10^{-18}	1×10^{-19}
Energetic distribution	Single	Single
Defect reference energy level Et	Above the highest EV	Above the highest EV
Characteristic energy (eV)	0.6	0.05
Total density (cm^3)	1×10^{10}	1×10^{10}

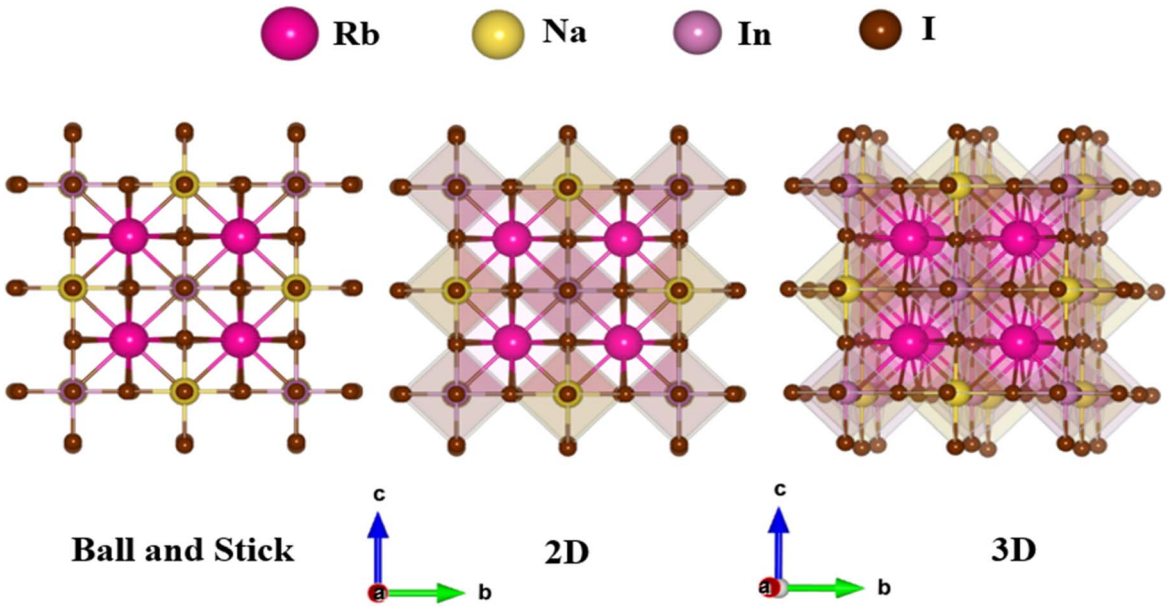

Fig. 3 Crystal structure of Rb_2NaInI_6.

environment. A crucial aspect of the structural stability of Rb_2NaInI_6 is its formation energy (ΔH_f), which serves as an indicator of thermodynamic feasibility. The negative formation energy of −1.238 eV per atom suggests that this material is energetically stable.[79,80] The formation energy was computed using the following equation:

$$\Delta H_f(Rb_2NaInI_6) = \frac{E_{tot}(Rb_2NaInI_6) - 2E_s(Rb) - E_s(Na) - E_s(In) - 6E_s(I)}{N} \quad (8)$$

where E_s (Rb), E_s (Na), E_s (In), and E_s (I) represent the individual atomic energies of Rb, Na, In, and I, respectively, while E_{tot} (Rb_2NaInI_6) denotes the total unit cell energy of the compound, and N signifies the number of atoms in the unit cell.[81]

Our computational findings align well with existing literature, reinforcing the validity and robustness of the adopted methodology. Evaluating the dynamic stability of a crystalline material is essential for determining its practical applicability, particularly under time-dependent or external perturbations. To this end, the phonon dispersion curve (PDC) serves as a critical diagnostic tool. In this study, we analyzed the dynamic behavior of Rb_2NaInI_6 by calculating its phonon spectrum along the high-symmetry paths (W–L–Γ–X–W–K) within the Brillouin zone, as depicted in Fig. 4. The absence of imaginary phonon

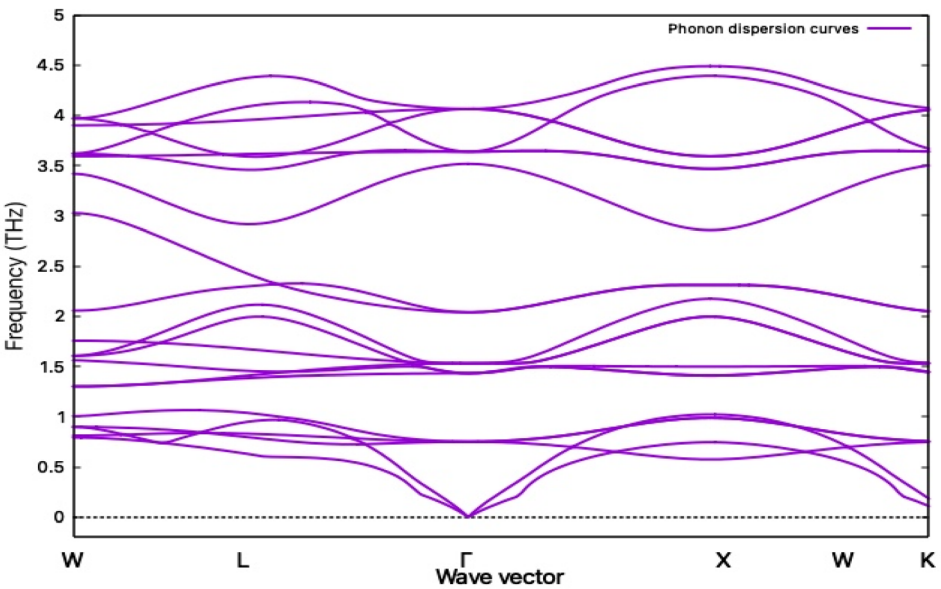

Fig. 4 Phonon dispersion spectrum of Rb_2NaInI_6.

modes across the entire Brillouin zone confirms the dynamical stability of the structure. This result is significant, as imaginary frequencies would indicate structural instabilities and potential lattice distortions. Therefore, the phonon dispersion analysis provides strong evidence that Rb_2NaInI_6 is not only energetically favorable but also dynamically stable, further supporting its potential for reliable real-world applications.

3.2. Band structure of Rb_2NaInI_6 compound

Understanding the electronic properties of a material is crucial in elucidating its bonding nature, photon absorption capabilities, and overall electronic behavior. One of the most significant aspects of these properties is the band structure, which provides insights into the energy levels that govern electrical conductivity and optical transitions. The band structure of Rb_2NaInI_6 was computed along the high-symmetry directions of the first Brillouin zone, as illustrated in Fig. 5. The Fermi level (E_F) is set at 0 eV and is indicated by a red dashed line. In this analysis, it is observed that neither the valence band (VB) nor the conduction band (CB) crosses the Fermi level, confirming the presence of an energy band gap in its electronic structure. The calculated band gap is 0.71 eV, suggesting that Rb_2NaInI_6 exhibits semiconducting behavior. Comparing this band gap with similar double perovskite compounds, it is noted that Rb_2NaInI_6 has a slightly lower band gap than $Rb_2CuSbBr_6$ (0.72 eV) but is higher than Rb_2CuSbI_6 (0.36 eV).[82] However, it is smaller compared to Rb_2ScInI_6 (0.90 eV)[83] and $Rb_2AgGaCl_6$ (1.28 eV).[84] A closer examination of the band structure reveals that the maximum of the valence band (VBM) and the minimum of the conduction band (CBM) are located at different *k*-points, confirming that Rb_2NaInI_6 is an indirect bandgap semiconductor. This characteristic typically results in lower radiative recombination rates, which could be advantageous or limiting, depending on the targeted application. Additionally, the valence band maximum (VBM) is found to be the closest to the Fermi level, which suggests that Rb_2NaInI_6 primarily exhibits p-type semiconducting behavior.[84,85] This is further supported by the presence of nearly flat valence bands between the *F* and *Z* points, which are observed close to the Fermi level. The high dispersion of these bands near E_F indicates a strong potential for high charge carrier mobility, suggesting that Rb_2NaInI_6 could have promising electrical transport properties. Moreover, the flat nature of some valence bands near E_F suggests a higher effective mass of charge carriers, which could influence hole transport dynamics. This balance between charge carrier mobility and effective mass is a key factor in determining the potential electronic and optoelectronic applications of Rb_2NaInI_6.[86]

3.3. DOS of Rb_2NaInI_6 compound

The total density of states (TDOS) and partial density of states (PDOS) provide critical insights into the electronic structure, chemical bonding, and orbital contributions in Rb_2NaInI_6. The TDOS, depicted in Fig. 6, shows a distribution of electronic states with a notable presence of approximately 12 electrons/eV at the Fermi level (E_F), marked by a vertical dashed line at 0 eV. This line distinguishes the valence band from the conduction band. Although the band structure reveals a finite band gap, the slight non-zero TDOS at E_F may suggest numerical broadening effects or indicate a semi metallic tendency within specific computational limits. In the valence band region ($E < 0$ eV), the I-5s and I-5p orbitals dominate the DOS, with secondary contributions from Rb-5s, Na-3s, and In-5p orbitals. The strong presence of I-5p and In-5p states reflects their critical role in chemical bonding and hole conduction, with the In–I interaction evident in the hybridized peaks. These features indicate

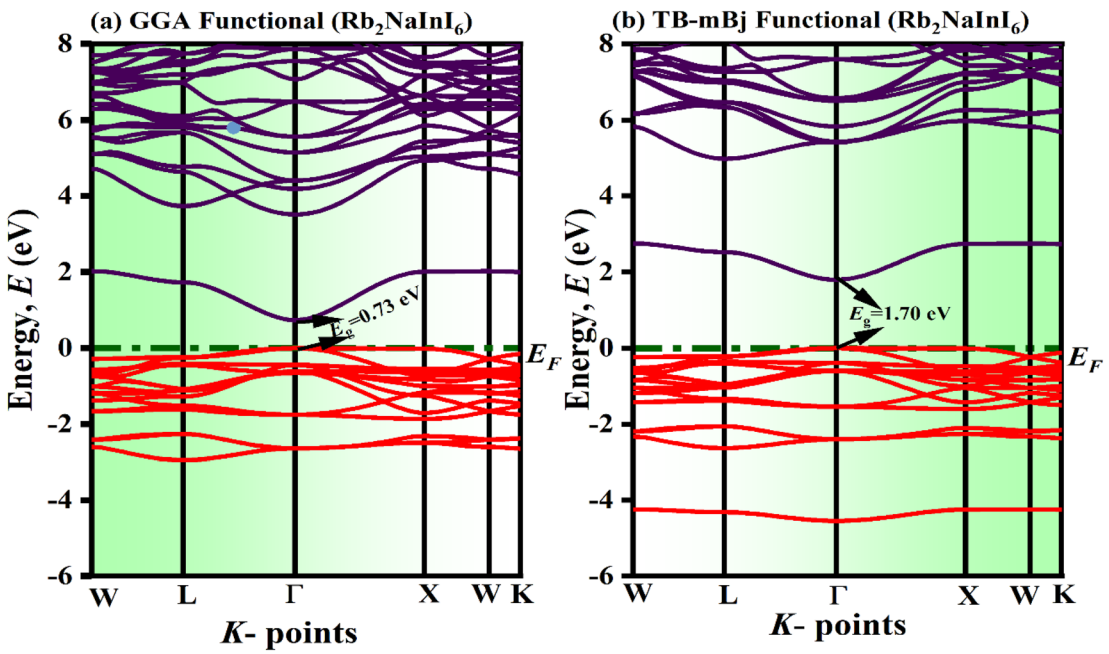

Fig. 5 Electronic band structure of Rb_2NaInI_6.

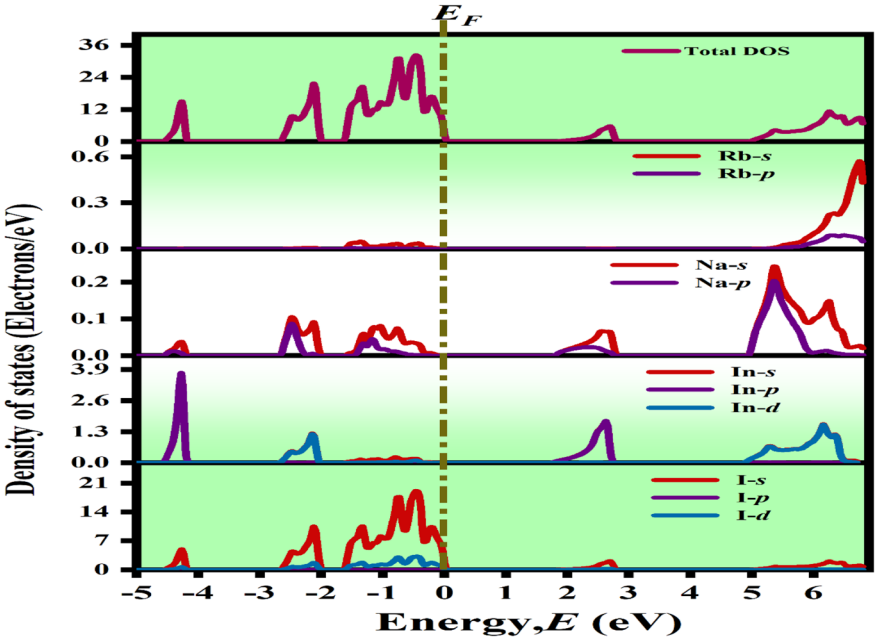

Fig. 6 Total and partial density of states of Rb_2NaInI_6.

substantial orbital overlap and suggest strong covalent character between Indium and Iodine atoms. In the conduction band ($E > 0$ eV), the DOS is primarily composed of In-5s, In-5p, and I-5p states, with additional minor contributions from Rb-5p and Na-3p orbitals. The sharp PDOS peaks observed in this region highlight discrete energy states, indicating well-defined

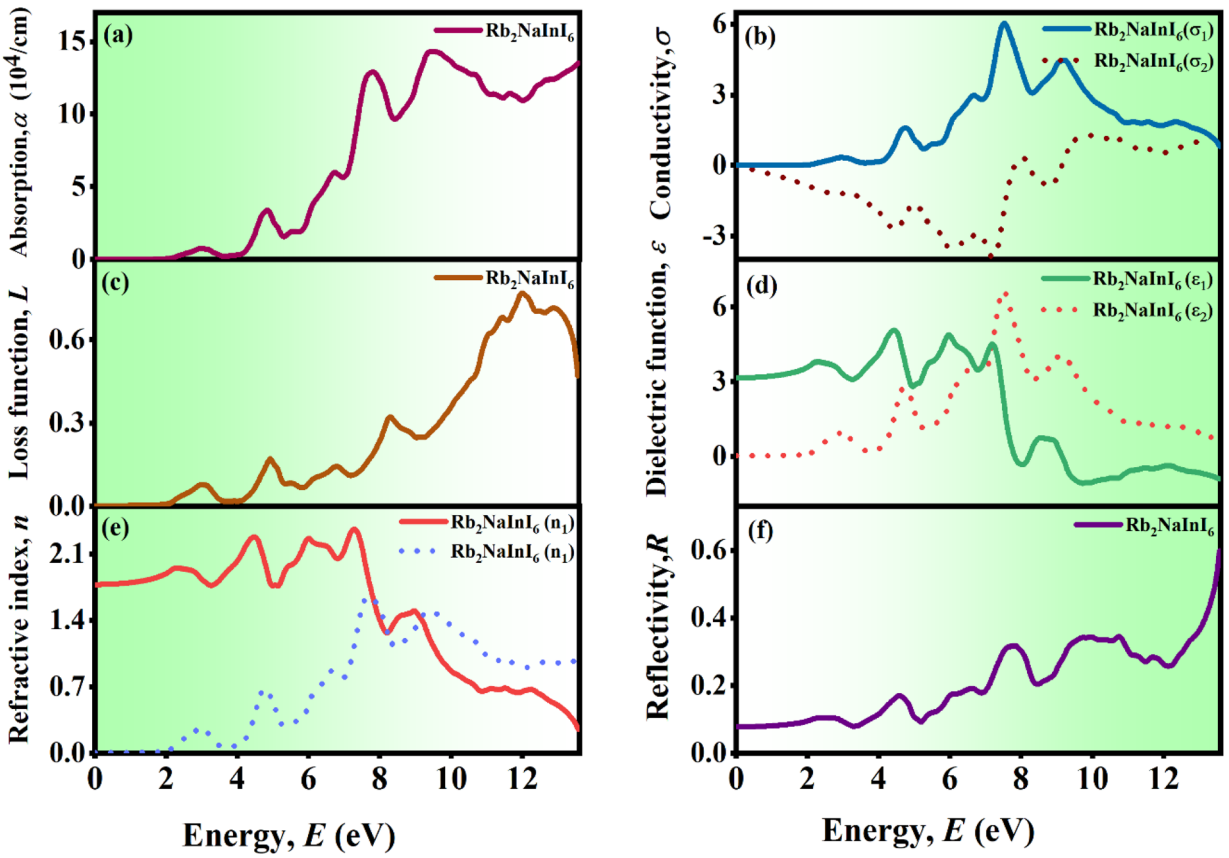

Fig. 7 Optical properties: (a) absorption, (b) loss function, (c) refractive index, (d) conductivity, (e) dielectric function, (f) reflectivity of Rb_2NaInI_6.

conduction channels. The overlapping of I-5p and In-5p states in both valence and conduction bands further emphasizes the degree of orbital hybridization, which plays a key role in enhancing electronic transitions and light absorption efficiency. Furthermore, while the d-orbitals of Indium and Iodine are less prominent, they do appear in the PDOS and contribute subtly to the deeper valence and higher conduction states, implying their involvement in electronic polarization and bonding symmetry adjustments. The overall orbital contributions, as mapped in the PDOS panels, reveal the intricate interplay between s, p, and d states, which collectively define the semiconducting nature and electronic behavior of Rb_2NaInI_6. These findings confirm that Rb_2NaInI_6 exhibits a suitable band gap, strong In–I orbital interactions, and well-structured electronic transitions, supporting its promise for optoelectronic and photovoltaic device applications.[87]

3.4. Optical properties of Rb_2NaInI_6 compound

Understanding the optical properties of a material is crucial for evaluating its interaction with electromagnetic waves, which directly influences its suitability for photovoltaic and optoelectronic applications.[88] The optical properties of Rb_2NaInI_6 are investigated over a broad range of photon energies, considering essential parameters such as absorption coefficient $\alpha(\omega)$, optical conductivity $\sigma(\omega)$, reflectivity $R(\omega)$, dielectric function $\varepsilon(\omega)$, refractive index $n(\omega)$ and energy loss function $L(\omega)$.

3.4.1. Absorption coefficient $\alpha(\omega)$. The absorption coefficient is a fundamental optical parameter that quantifies how deeply incident light penetrates a material before being absorbed. A high absorption coefficient is desirable for applications such as solar cells and photodetectors.[89] The calculated absorption spectrum of Rb_2NaInI_6 shows strong absorption in the visible to ultraviolet (UV) region, making it highly efficient in capturing solar energy. The initial peak in the absorption spectrum is observed at 1.70 eV, aligning with the bandgap value calculated using the TB-mBJ functional. As photon energy increases, the absorption intensity rises markedly, reaching a maximum of approximately 1.5×10^4 cm^{-1}, which signifies strong photon absorption in the ultraviolet region and highlights the material's suitability for optoelectronic applications (Fig. 7).

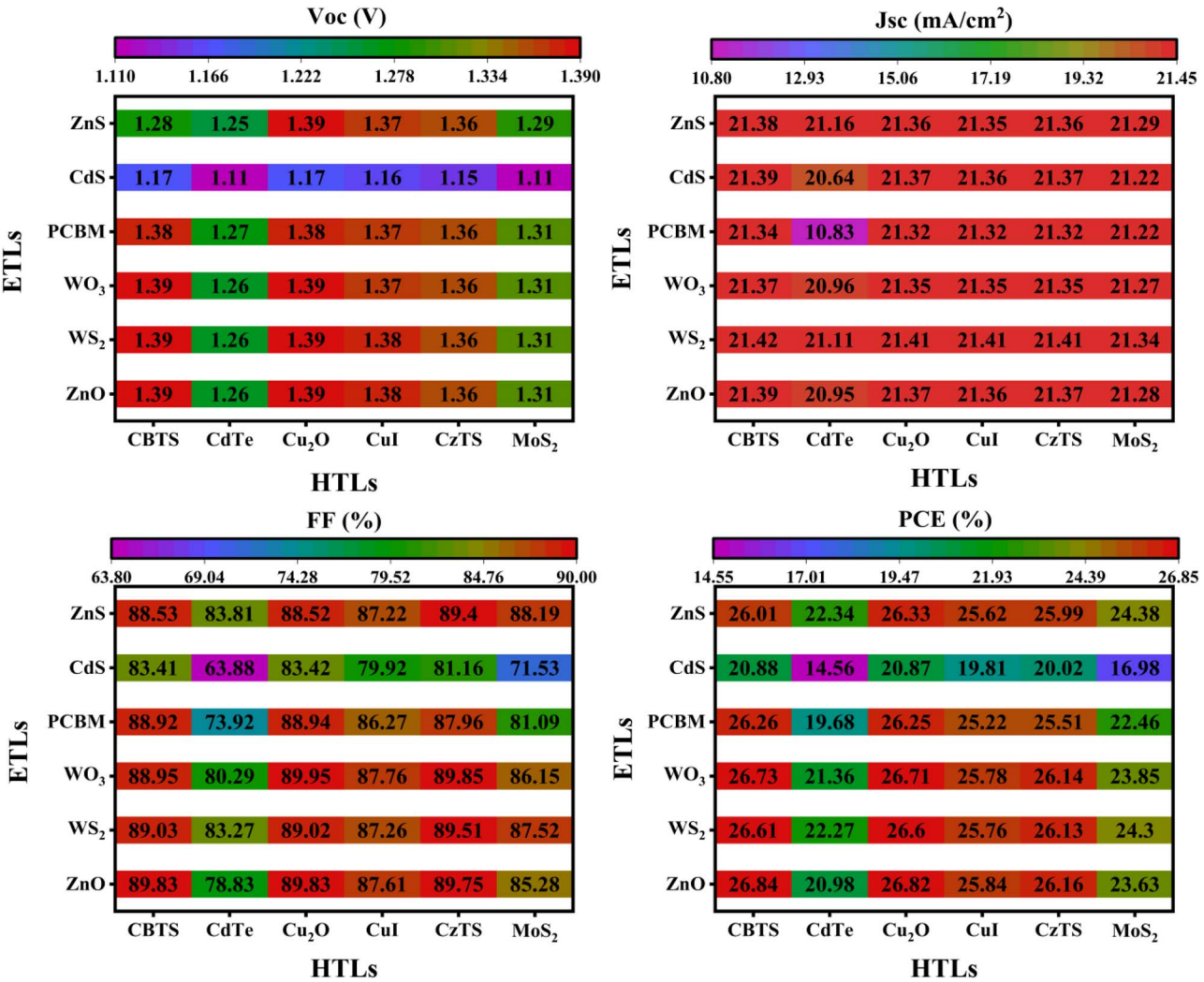

Fig. 8 Performance parameters of Variation. *i.e.* V_{oc} (V), J_{sc} (mA cm^{-2}), FF (%), PCE (%) of Rb_2NaInI_6 absorber layer.

3.4.1.1 Optical conductivity σ(ω). The optical conductivity represents the ability of free charge carriers to respond to an applied electric field within specific energy ranges.[90] The optical conductivity spectrum of Rb_2NaInI_6 remains negligible at low photon energies due to its semiconducting nature. The optical conductivity (σ_1) begins to rise noticeably around 6 eV, reaching a distinct peak at approximately 7.5 eV, followed by a steady decline toward near-zero values. This spectral behavior indicates a high degree of photoresponsivity in Rb_2NaInI_6, underscoring its potential for integration into optoelectronic devices, including photodetectors and light-emitting components.

3.4.1.2 Reflectivity R(ω). Reflectivity is an important property that determines how much of the incident light is reflected off the surface of the material.[91] The reflectivity spectrum of Rb_2NaInI_6 starts with a low value of ~7% at 0 eV, which ensures high light absorption and minimal optical losses—a crucial requirement for solar cell applications. The reflectivity increases with energy, reaching a peak of approximately 60% around 13.6 eV, which is attributed to interbond transitions. However, the overall reflectance remains below 65%, indicating that Rb_2NaInI_6 is an excellent absorber of light.

3.4.2. Dielectric function ε(ω). The dielectric function characterizes the optical response of a material when subjected to an electromagnetic field. It consists of a real part $\varepsilon_1(\omega)$, which represents the material's ability to store electric energy, and an imaginary part $\varepsilon_2(\omega)$, which corresponds to energy absorption due to electronic transitions.[92] The static dielectric constant $\varepsilon_1(\omega)$ of Rb_2NaInI_6 is relatively high, indicating efficient charge separation, which is beneficial for photovoltaic and optoelectronic applications. The real part $\varepsilon_1(\omega)$ of the dielectric function exhibits a marked decline beyond 7 eV, suggesting the onset of metallic behavior at elevated photon energies. Meanwhile, the imaginary component $\varepsilon_2(\omega)$ shows a pronounced peak near 8 eV, indicative of intense interband electronic transitions within the material.

3.4.2.1 Refractive index n(ω). The refractive index characterizes the degree to which light is bent as it passes through a material. For Rb_2NaInI_6, the static refractive index $n_1(\omega)$ exhibits fluctuations in the photon energy range of 2 to 8 eV, with a pronounced peak near 7.7 eV, indicating a strong light–matter interaction. The imaginary component $n_2(\omega)$ remains relatively high up to approximately 8 eV, supporting the material's potential use in infrared sensors, waveguides, and optical coating applications. Beyond 8 eV, both real and imaginary parts of the refractive index begin to decline, with $n_2(\omega)$ approaching unity around 12 eV, which confirms the material's optical transparency in the ultraviolet region.[93]

3.4.3. Loss function L(ω). The energy loss function describes the loss of energy due to electron interactions in the material.[94] The plasma frequency ω_p, which represents the energy level at which the material transitions from a dielectric to a metallic state, is identified at approximately 12 eV. This

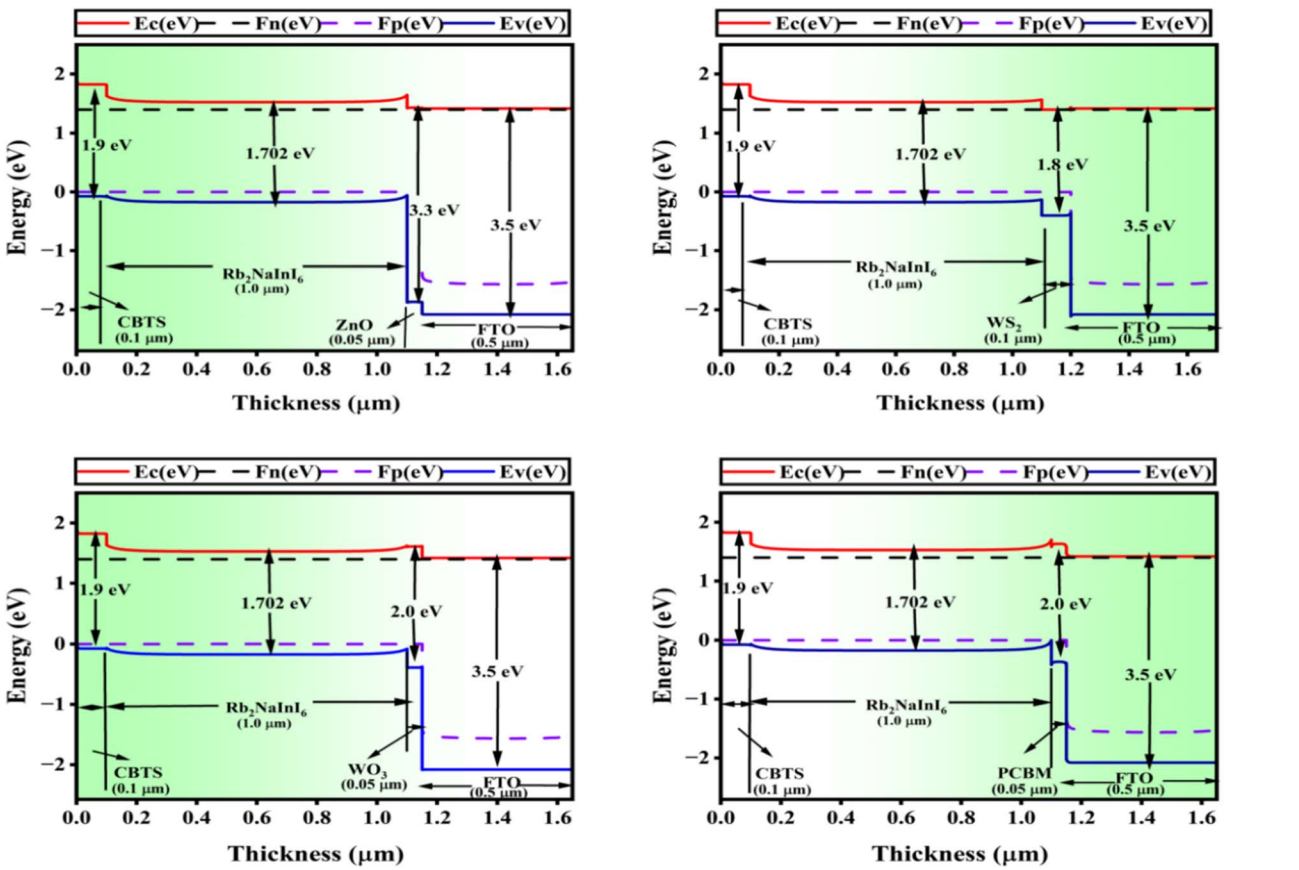

Fig. 9 Band diagram illustrating Rb_2NaInI_6, (a) ZnO, (b) WS_2, (c) WO_3, and (d) PCBM are the first four.

suggests that Rb_2NaInI_6 exhibits excellent stability in the visible and infrared range while showing metallic behavior in the ultraviolet region. The primary loss peak confirms its ability to be used in high-frequency optical applications.[95]

3.5. Evaluation of SCAPS 1D outcomes

3.5.1. Optimization of ETL and HTL material combinations for enhanced photovoltaic performance. In solar cell design, the selection of electron transport layer (ETL) and hole transport layer (HTL) materials plays a critical role in determining the device's overall performance. These transport layers not only facilitate efficient extraction and transport of charge carriers (electrons and holes) but also significantly influence the open-circuit voltage (V_{oc}), short-circuit current density (J_{sc}), fill factor (FF), and power conversion efficiency (PCE). An optimal ETL/HTL combination ensures minimal recombination losses, good energy level alignment with the absorber, and high carrier mobility, all of which are essential for achieving superior device efficiency and stability. In this context, Fig. 8 presents a comparative performance analysis of different ETL and HTL materials using Rb_2NaInI_6 as the absorber layer, with a focus on four key parameters: V_{oc}, J_{sc}, FF, and PCE. To select the best ETL materials, the HTL CBTS was considered, as it consistently demonstrated strong performance across various ETL combinations. Among the ETLs, ZnO stood out with the highest PCE of 26.84%, coupled with a V_{oc} of 1.39 V, J_{sc} of 21.39 mA cm^{-2}, and FF of 89.83%. These parameters indicate excellent charge extraction capability, minimal energy losses, and strong interfacial contact with CBTS, making ZnO an outstanding candidate. WS_2 also exhibited remarkable performance, achieving a PCE of 26.61%, V_{oc} of 1.39 V, J_{sc} of 21.42 mA cm^{-2}, and FF of 89.03%. The layered structure and good electrical conductivity of WS likely contribute to its efficient charge transport and collection, further validating its suitability. WO_3 emerged as another high-performing ETL, delivering a PCE of 26.73%, V_{oc} of 1.39 V, J_{sc} of 21.37 mA cm^{-2}, and FF of 88.95%. WO_3's high work function and excellent electron affinity promote efficient electron extraction while suppressing recombination at the interface. Similarly, PCBM demonstrated strong performance with a PCE of 26.26%, V_{oc} of 1.38 V, J_{sc} of 21.34 mA cm^{-2}, and FF

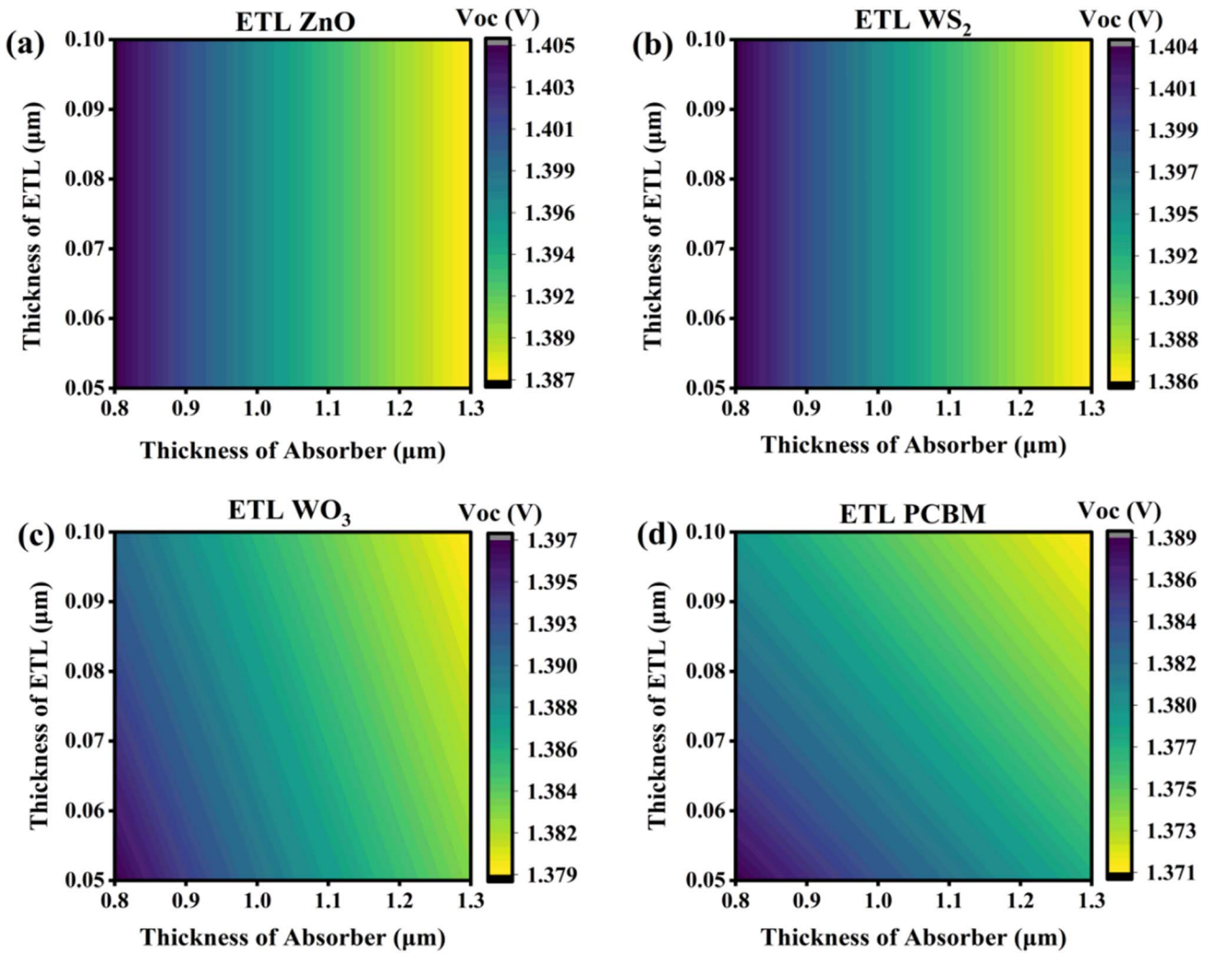

Fig. 10 Contour modeling of the V_{oc} (V) with the HTL-like (a) ZnO, (b) WS_2, (c) WO_3, (d) PCBM.

of 88.92%. Although slightly lower in FF compared to the top three, PCBM still offers a robust balance of parameters and good compatibility with the CBTS HTL. The consistent performance of these ETL materials in combination with CBTS highlights their strong interfacial alignment, effective charge transport properties, and potential to enhance the overall device efficiency. In summary, the careful evaluation of performance metrics from Fig. 8 justifies the selection of ZnO, WS_2, WO_3, and ZnS as the four best ETL materials when paired with CBTS, underscoring the importance of synergistic ETL/HTL combinations in optimizing perovskite solar cell performance.

3.5.2. Interactions of conduction band offset (CBO) as well as valence band offset (VBO). Band offsets, the conduction band offset (CBO) along with the valence band offset (VBO), are essential for comprehending the behavior of charge transporters in thin-film perovskite solar energy cells (PSCs), as emphasized in an overview. The CBO denotes the energy disparity across the conductive band of the electron transport layer (CTL) while participating in the absorber material, whereas the VBO indicates the variation in energy concerning the valence band, or band, in the CTL when the perovskite absorbers, furthermore, ref. 96 Clarifies the energy level requirements for efficient hole extraction and electron blocking in perovskite solar cells. To ensure efficient hole extraction from the perovskite absorber to the hole transport layer (HTL), the highest occupied molecular orbital (HOMO) of the perovskite should indeed be slightly higher (less damaging) than the HOMO of the HTL, as this energy level alignment facilitates the movement of holes from a higher state of energy to a minimal energy state. To inhibit the flow of electrons from the perovskite's LUMO (lower unoccupied molecular orbital) through the hole transport layer (HTL), a substantial energy disparity separating the perovskite's LUMO and the power levels of the HTL is advantageous. This electrical barrier effectively obstructs the movement of electrons to the HTL, thereby enhancing charge separation and minimizing recombination losses. Therefore, carefully adjusting the valence band offset (VBO) and conduction band offset (CBO) at the perovskite/HTL interface is indeed a critical factor in achieving efficient hole extraction and overall high performance in perovskite solar cells, making the optimization of these band offsets through material selection and interface engineering a key focus in the field.[97] The Conduction Band Offset (CBO) and Valence Band Offset (VBO) can be optimized by using the relations,

$$\mathrm{CBO} = X_{\mathrm{absorber}} - X_{\mathrm{ETL}} \tag{9}$$

$$\mathrm{VBO} = X_{\mathrm{HTL}} - X_{\mathrm{absorber}} + \mathrm{Eg}_{\mathrm{HTL}} - \mathrm{Eg}_{\mathrm{absorber}} \tag{10}$$

To determine the conduction band offset (CBO) and valence band offset (VBO), eqn (8) and (9) can be employed. For instance, when considering WS_2, the CBO at the electron transport layer (ETL)/absorber interface can be calculated using

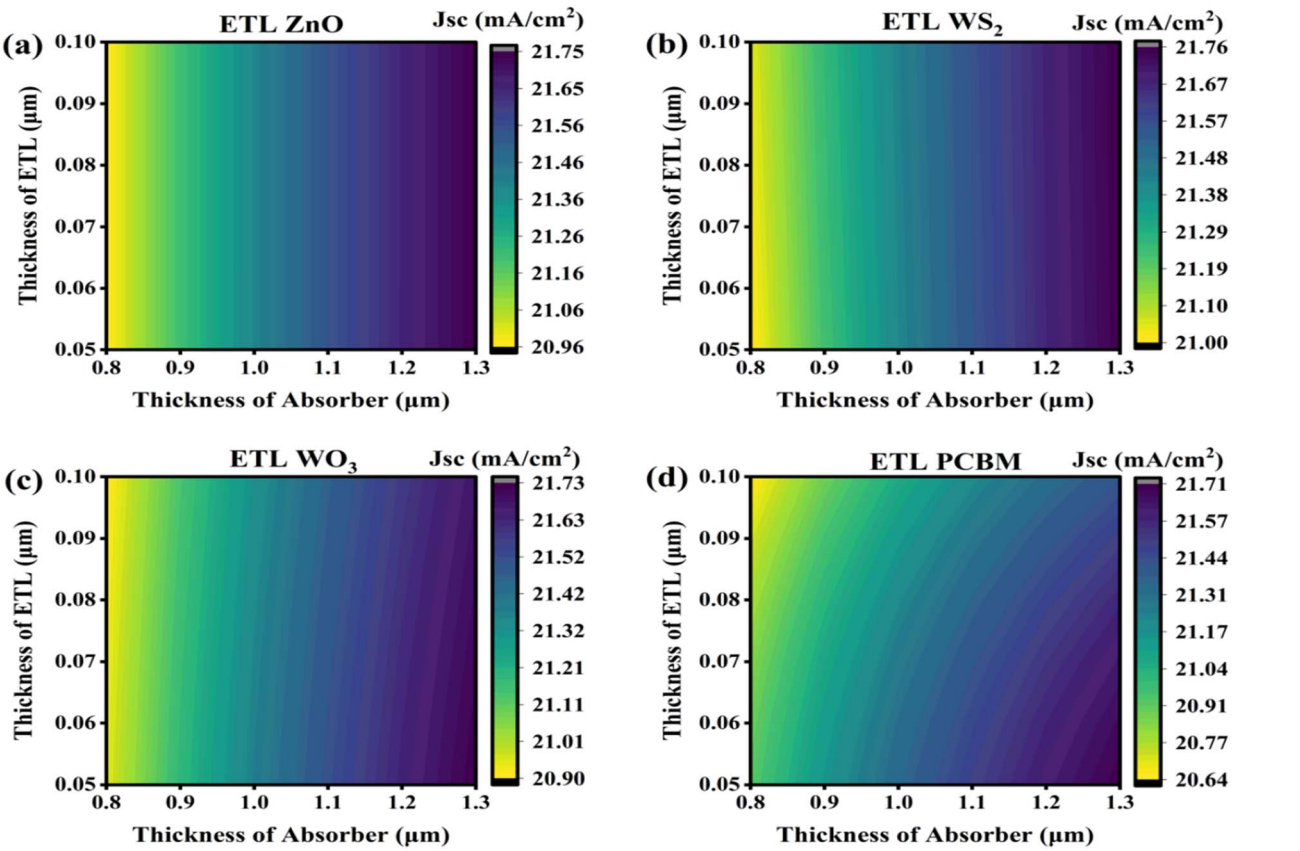

Fig. 11 Contour modeling of the J_{sc} (mA cm^{-2}) with the HTL-like (a) ZnO, (b) WS_2, (c) WO_3, (d) PCBM.

these equations. $X_{absorber} - X_{ETL} = 3.779–3.95 = -0.171$ eV = CBO. The computed negative CBO value illustrates a cliff-like power barrier at the interface of the system. VBO is equal to $X_{HTL} - X_{absorber} + Eg_{HTL} - Eg_{Absorber} = 3.6–3.779 + 1.9–1.702 =$ 0.019 eV. The absorber/HTL contact at the valence band offset. A positive CBO value indicates the existence of a spike-like energetic barrier. The VBO remained consistent at 0.019 eV across all ETLs. The CBO values varied depending on the ETL: −0.171 eV for WS_2, −0.2998 eV for WO_3, −1.598 eV for ZnO, and −0.298 eV for PCBM. The VBO CBO table is attached in the supporting information.

3.5.3. Band diagram. Fig. 9a–d illustrates the energy band diagrams of the simulated FTO/ETL/Rb_2NaInI_6/CBTS solar cells, highlighting the crucial energy level alignment at the ETL-Rb_2NaInI_6 and Rb_2NaInI_6-CBTS interfaces for efficient charge extraction. For effective electron extraction, the electron affinity of the ETL must be higher than that of the Rb_2NaInI_6 absorber, In each diagram, the quasi-Fermi levels for electrons (F_n) and holes (F_p) are shown relative to the conduction band (E_c) and valence band (E_v) energies, indicating the energy landscape for photogenerated carrier transport. The Rb_2NaInI_6 absorber has a band gap of approximately 1.7–1.8 eV (inferred from the diagrams), while the band gaps of the ZnO, WS_2, WO_3, and PCBM ETLs. The varying band alignments and offsets presented in Fig. 9a–d likely contribute to the differences in V_{oc} and FF observed for the different ETLs, underscoring the importance of selecting an ETL with optimal energy level matching to both the absorber and the front contact for enhanced charge extraction and overall device efficiency. Further analysis of the specific band offsets and their correlation with device performance metrics is necessary to identify the most promising ETL for this solar cell architecture.

3.5.4. Integrate the effects of absorber and then ETL thickness in photovoltaic cells made from perovskite. The thickness of both the absorber layer and the electron transport layer (ETL) is a key determinant of solar cell performance, and overall energy conversion efficiency. Achieving optimal photovoltaic performance requires precise control over the thickness of these layers. In particular, the ETL thickness must be fine-tuned to avoid excessive light absorption and to enhance photon penetration into the absorber layer.[98] For high-efficiency solar cells, the entire PV structure must be carefully engineered and optimized.[97] Fig. 10 illustrates the open-circuit voltage (V_{oc}) variations of contour maps as a function of absorber and electron transport layer (ETL) thickness for solar cells with different ETLs: (a) FTO/ZnO/Rb_2NaInI_6/CBTS, (b) FTO/WS_2/Rb_2NaInI_6/CBTS, (c) FTO/WO_3/Rb_2NaInI_6/CBTS, and (d) FTO/PCBM/Rb_2NaInI_6/CBTS. For FTO/ZnO/Rb_2NaInI_6/CBTS (Fig. 10a), the V_{oc} ranges from 1.387 V to 1.405 V, with the highest values observed at a thinner absorber layer, below 0.8 μm. This suggests that reducing layer thickness enhances charge separation and minimizes recombination. A similar trend is observed for FTO/

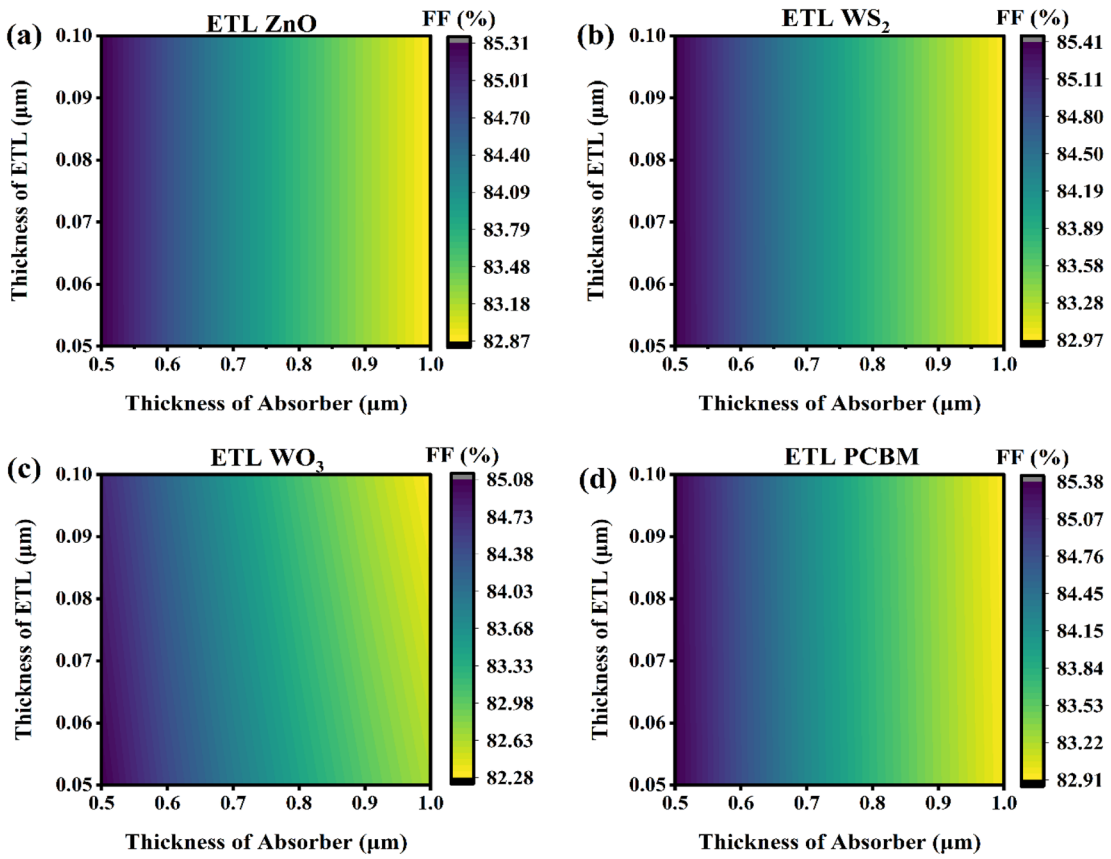

Fig. 12 Contour modeling of the FF(%) with the HTL-like (a) ZnO, (b) WS_2, (c) WO_3, (d) PCBM.

WS_2/Rb_2NaInI_6/CBTS (Fig. 10b), where V_{oc} values upscale from 1.386 V to 1.404 V, though the slightly narrower range compared to ZnO indicates differences in interfacial properties that could affect charge transport efficiency. In the case of FTO/WO_3/Rb_2NaInI_6/CBTS (Fig. 10c), V_{oc} values range between 1.379 V and 1.397 V. A minimal absorber thickness (0.8 μm) and thinner ETL (0.05–0.06 μm) needed for achieving highest V_{oc}, which are slightly lower than those for ZnO and WS_2, possibly due to increased charge recombination or less efficient charge extraction at the interface. FTO/PCBM/Rb_2NaInI_6/CBTS (Fig. 10d) exhibits the lowest V_{oc} values, ranging from 1.371 V to 1.389 V, indicating that charge transport limitations or higher interfacial recombination might be negatively impacting performance. However, the ETL material selection also plays a critical role in device performance, with FTO/ZnO/Rb_2NaInI_6/CBTS and FTO/WS_2/Rb_2NaInI_6/CBTS demonstrating superior V_{oc} values compared to FTO/WO_3/Rb_2NaInI_6/CBTS and FTO/PCBM/Rb_2NaInI_6/CBTS. Contour maps show that an absorber thickness of 1.2–1.3 μm yields the highest J_{sc}, highlighting the need for precise thickness optimization. Overall, selecting a suitable ETL and tuning absorber and HTL thicknesses are key to achieving high-efficiency solar cells.

Fig. 11a–d presents contour plots illustrating the short-circuit current density (J_{sc}) of FTO/ETL/Rb_2NaInI_6/CBTS-based solar cells as a function of both absorber (Rb_2NaInI_6) as well as ETL thicknesses for four different ETLs: ZnO, WS_2, WO_3, and PCBM. Across all cases, J_{sc} consistently increases with absorber thickness, particularly in the 1.2–1.3 μm range, as thicker absorbers enhance light absorption and electron–hole pair generation. For the FTO/ZnO/Rb_2NaInI_6/CBTS (Fig. 11a) structure, J_{sc} ranges from ~20.96 to 21.75 mA cm^{-2}, with slightly higher values observed at thinner ETLs and thicker absorbers. The FTO/WS_2/Rb_2NaInI_6/CBTS (Fig. 11b) structure depicts the highest performance, achieving J_{sc} values from ~21.00 to 21.76 mA cm^{-2}, indicating that WS_2 gives more efficient electron extraction as well as transport. The FTO/WO_3/Rb_2NaInI_6/CBTS (Fig. 11c) configuration shows a similar trend, with J_{sc} ranging between ~20.90 and 21.73 mA cm^{-2}, showing minimal sensitivity to ETL thickness. Meanwhile, the FTO/PCBM/Rb_2NaInI_6/CBTS (Fig. 11d) device displays a wider but slightly lower J_{sc} range of ~20.64 to 21.71 mA cm^{-2}, with the absorber thickness again playing the dominant role. The Rb_2NaInI_6 absorber thickness is the key factor in maximizing J_{sc}, with WS_2 proving to be the most effective ETL for enhancing current and overall performance. Contour maps show that an absorber thickness of 1.2–1.3 μm consistently yields the highest J_{sc}, highlighting the need for precise optimization. Overall, selecting a suitable ETL and fine-tuning absorber and HTL thicknesses are vital for achieving high-efficiency solar cells, with WS_2 emerging as the most promising choose.

The contour plots in Fig. 12a–d illustrate the fill factor (FF) dependency on the thickness of the ETL and absorber layer for FTO/ETL/Rb_2NaInI_6/CBTS solar cells. The FF, which represents the efficiency of charge extraction and recombination losses,

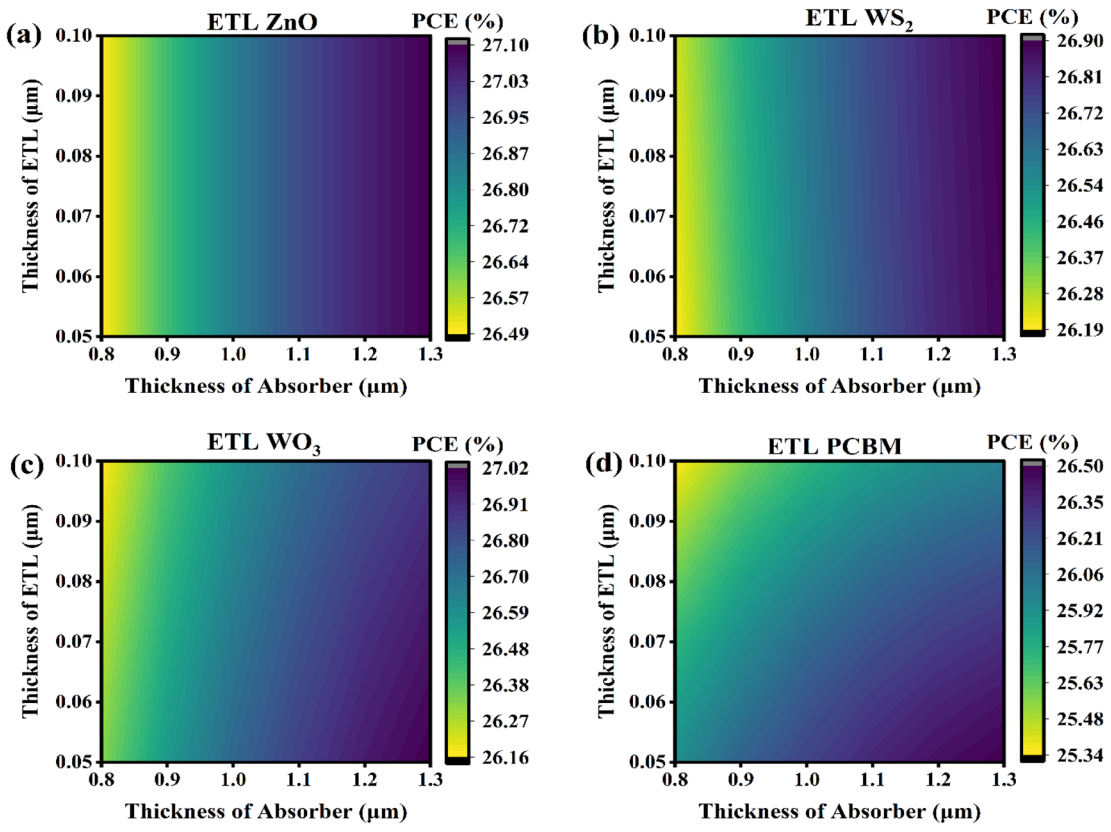

Fig. 13 Contour mapping of PCE (%) when ETL is (a) ZnO, (b) WS_2, (c) WO_3, (d) PCBM.

exhibits the highest values for thinner absorber layers (0.5–0.6 μm) across all SCs, indicating improved charge transport with reduced recombination. Among the devices, WS_2-based SC (Fig. 12c) demonstrates the best FF performance, peaking at 85.41%, followed by PCBM/Rb_2NaInI_6/CBTS (Fig. 12d) (85.38%), ZnO/Rb_2NaInI_6/CBTS (Fig. 12a) (85.31%), and WO_3/Rb_2NaInI_6/CBTS (Fig. 12c) the lowest (85.08%). ETL thicknesses between 0.05–0.07 μm are optimal, as thicker layers increase resistive losses and hinder charge transport. FF declines when absorber thickness exceeds 0.8 μm, likely due to higher recombination and reduced carrier collection. WS_2 emerges as the most effective ETL for high FF, with PCBM also showing competitive performance.

Fig. 13 shows that the contour plots as a function of Power Conversion Efficiency (PCE) (%) both absorber (Rb_2NaInI_6) and Electron Transport Layer (ETL) thickness for four different solar cell configurations: FTO/ZnO/Rb_2NaInI_6/CBTS, FTO/WS_2/Rb_2NaInI_6/CBTS, FTO/WO_3/Rb_2NaInI_6/CBTS, and FTO/PCBM/Rb_2NaInI_6/CBTS. Across all four architectures, PCE increases noticeably with increasing absorber thickness, particularly in the range of 1.2–1.3 μm, due to enhanced photon absorption and improved generation of charge carriers. The FTO/ZnO/Rb_2NaInI_6/CBTS (Fig. 13a) device exhibits PCE values ranging from 26.49% to 27.10%, peaking with a thinner ZnO layer (0.05–0.07 μm) and a thicker absorber. The FTO/WS_2/Rb_2NaInI_6/CBTS (Fig. 13b) configuration, although not reaching the absolute highest value, achieves a very consistent performance across thickness variations, with PCEs from 26.19% to 26.90%, highlighting WS_2 as an excellent ETL candidate due to its stable and efficient electron transport. The FTO/WO_3/Rb_2NaInI_6/CBTS (Fig. 13c) device reaches up to 27.02% PCE, again performing best with absorber thickness of 1.2–1.3 μm and thin WO_3 layers (0.05–0.07 μm). In contrast, the FTO/PCBM/Rb_2NaInI_6/CBTS (Fig. 13d) structure shows a slightly lower performance, ranging from 25.34% to 26.50%, with its optimum appearing at a somewhat thicker ETL (0.07–0.1 μm) and a comparable absorber thickness, suggesting a more nuanced relationship between layer thickness and efficiency. Overall, this analysis underscores the critical role of optimizing absorber thickness to enhance light absorption and subsequently improve solar cell efficiency, while also indicating that careful selection and thickness control of the ETL are necessary for maximizing charge transport and overall device performance.[99,100]

3.5.5. Combine effect of shallow acceptor density and defect density. In perovskite solar cells, absorber defect density (N_t) refers to the density of traps or imperfections within the

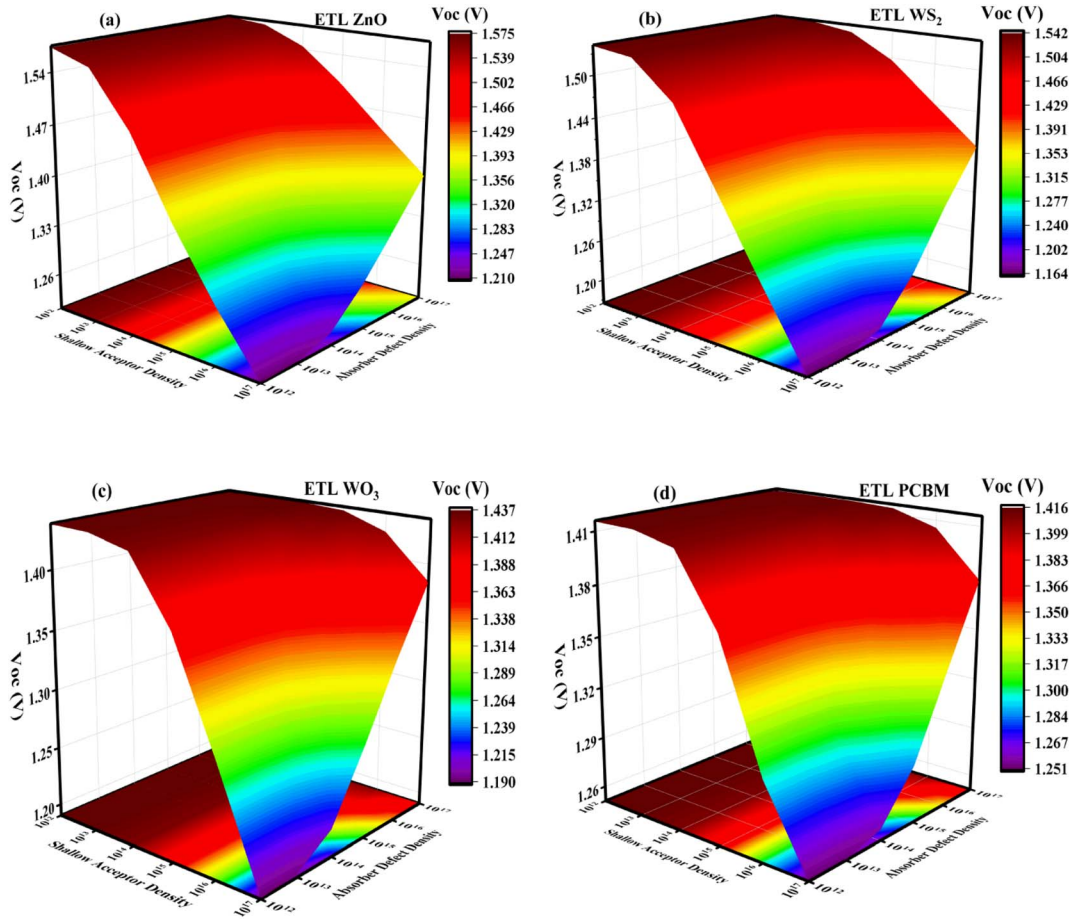

Fig. 14 Three-dimensional surface plot of both open-circuit voltage (V_{OC}) being a function of shallow acceptor density (N_A) in addition to absorber defect density (N_D) for perovskite solar cells (PSCs) utilizing (a) ZnO, (b) WS_2, (c) WO_3, and (d) PCBM electron transport layers (ETLs).

perovskite layer that can capture and recombine charge carriers. In contrast, shallow acceptor density (N_a) refers to intentional p-type doping that adds mobile holes to facilitate the modulation of the electrical characteristics of the material that absorbs radiation. When you combine these two factors, the interaction between them strongly influences the device's key performance metrics: open-circuit voltage (V_{oc}), short-circuit current density (J_{sc}), fill factor (FF), and overall power conversion efficiency (PCE).[98,99] The combined effect of absorber defect density and shallow acceptor density on photovoltaic (PV) performance is illustrated in Fig. 14–17. In these figures, the defect density varied from 10^{12} to 10^{17}, while the acceptor density exhibited a similar trend.

The four 3D surface plots (Fig. 14a–d) illustrate the combined impact of shallow acceptor density (N_A) and absorber defect density (N_t) on the open-circuit voltage (V_{oc}) of perovskite solar cells (PSCs) employing different electron transport layers (ETLs): ZnO-based device (Fig. 14a), WS_2-based device (Fig. 14b), WO_3-based device (Fig. 14c), and PCBM-based device (Fig. 14d). Across all ETLs, a clear trend emerges: as the absorber defect density (N_t) increases, V_{oc} consistently decreases due to enhanced non-radiative recombination, which reduces the quasi-Fermi level splitting and ultimately lowers the open-circuit potential. In contrast, increasing the shallow acceptor density (N_A) generally leads to an increase in V_{oc}, thanks to the stronger built-in electric field that improves charge separation and reduces recombination. The optimal condition for maximizing V_{oc} is a low N_t ($<10^{13}$ cm^{-3}) combined with intermediate-to-high N_A (10^{15}–10^{16} cm^{-3}). At very high N_A levels, V_{oc} may plate Pt or slightly decline due to adverse effects such as increased Ptger recombination or impaired carrier mobility. Specifically, for the ZnO-based device (Fig. 14a), V_{oc} ranges from approximately 1.21 V to 1.575 V; for the WS_2-based device (Fig. 14b), it spans about 1.164 V to 1.542 V; for the WO_3-based device (Fig. 14c), it ranges from ~1.190 V to 1.437 V; and for the PCBM-based device (Fig. 14d), it shows the lowest maximum V_{oc}, between ~1.251 V and 1.416 V. This analysis suggests that ZnO and WS_2 are the most favorable ETLs for

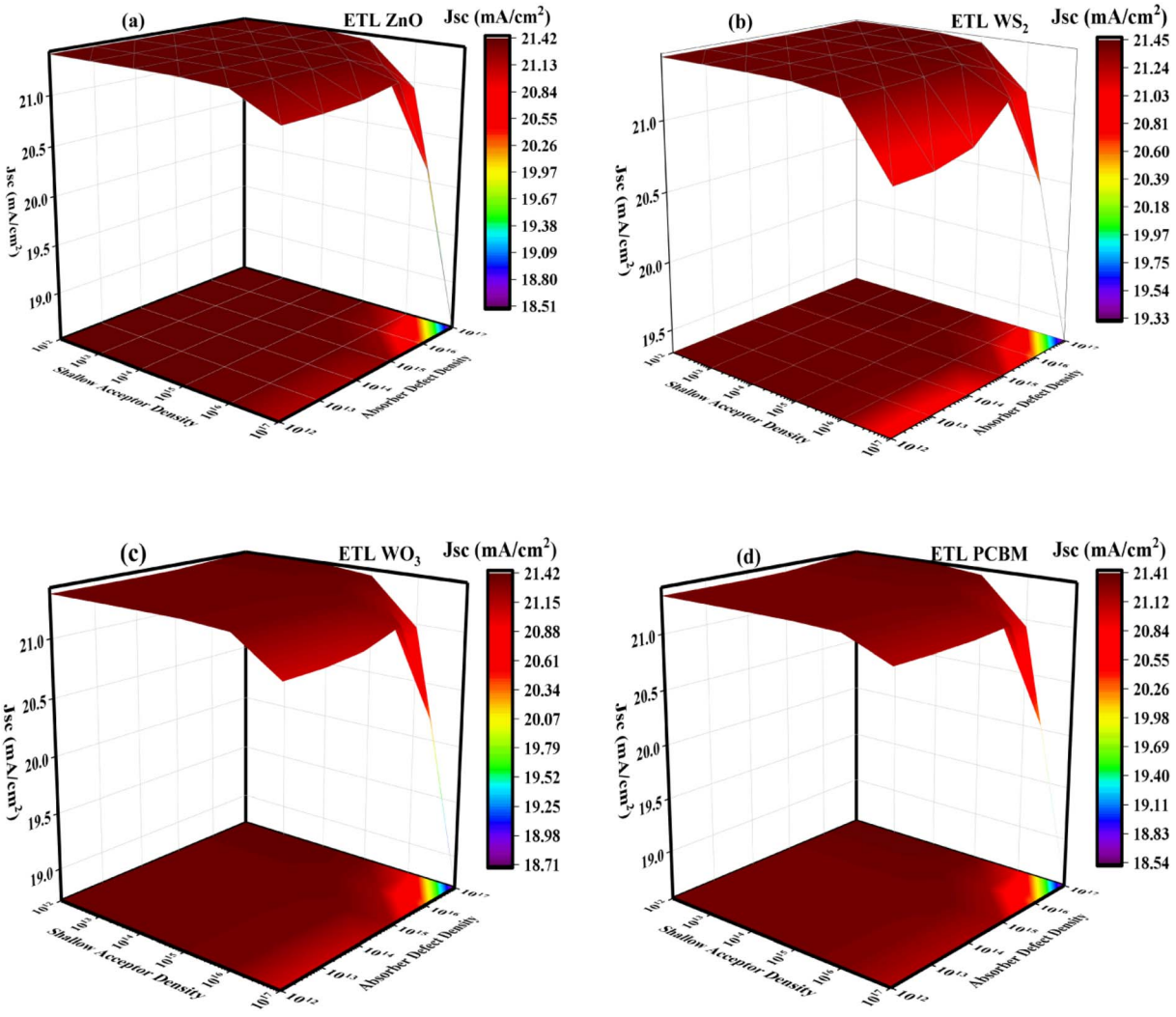

Fig. 15 Three-dimensional surface plot of both short-circuits voltage (J_{sc}) being a function of shallow acceptor density (N_A) in addition to absorber defect density (N_D) for perovskite solar cells (PSCs) utilizing (a) ZnO, (b) WS_2, (c) WO_3, and (d) PCBM electron transport layers (ETLs).

achieving high open-circuit voltages, especially in scenarios of minimal number of defects and enhanced doping.

Fig. 15a–d illustrates how shallow acceptor density (N_A) and absorber defect density (N_t) influence the short-circuit current density (J_{sc}) of PSCs across four configurations. Overall, J_{sc} shows a strong negative dependence on absorber defect density (N_t), as higher defect densities introduce recombination centers that reduce the collection of photogenerated carriers. Unlike V_{oc}, J_{sc} is less sensitive to variations in shallow acceptor density (N_A), though moderate improvements are sometimes observed at intermediate to high N_A, likely due to better charge extraction. However, excessively high doping levels may slightly decrease J_{sc}, potentially becPtse of enhanced carrier scattering or mobility limitations. For the ZnO-based device (Fig. 15a), J_{sc} ranges from approximately 19 to 20 A m^{-2}, with similar values seen for the WS_2-based device (Fig. 15b), WO_3-based device (Fig. 15c), and PCBM-based device (Fig. 15d). Across all ETLs, minimizing absorber defect density emerges as the most critical factor in maximizing J_{sc}, underscoring the importance of material quality and defect passivation strategies in high-performance PSC designs.

The combined effect of absorber defect density (N_t) and shallow acceptor density (N_A) on the fill factor (FF) of perovskite photovoltaic cells, shown in Fig. 16a–d, demonstrates that FF is moderately sensitive to both parameters, though less dramatically than V_{oc}. The analysis of the fill factor (FF) plots reveals that the ZnO-based device exhibits the highest FF values (~90–91%) when the shallow acceptor density (N_A) is in between 10^{16} and 10^{17} cm^{-3}, provided the absorber defect density (N_t) remains below 10^{15} cm^{-3}. This indicates that the ZnO ETL can maintain excellent carrier extraction and minimize recombination even at relatively high doping levels, as long as defect densities are kept low. In contrast, WS_2 (Fig. 16b), WO_3-(Fig. 16c), and PCBM-based (Fig. 16d) devices show initial FF values above ~91%, which decline to ~67–73% at the highest N_t and N_A regions. This decline can be attributed to enhanced

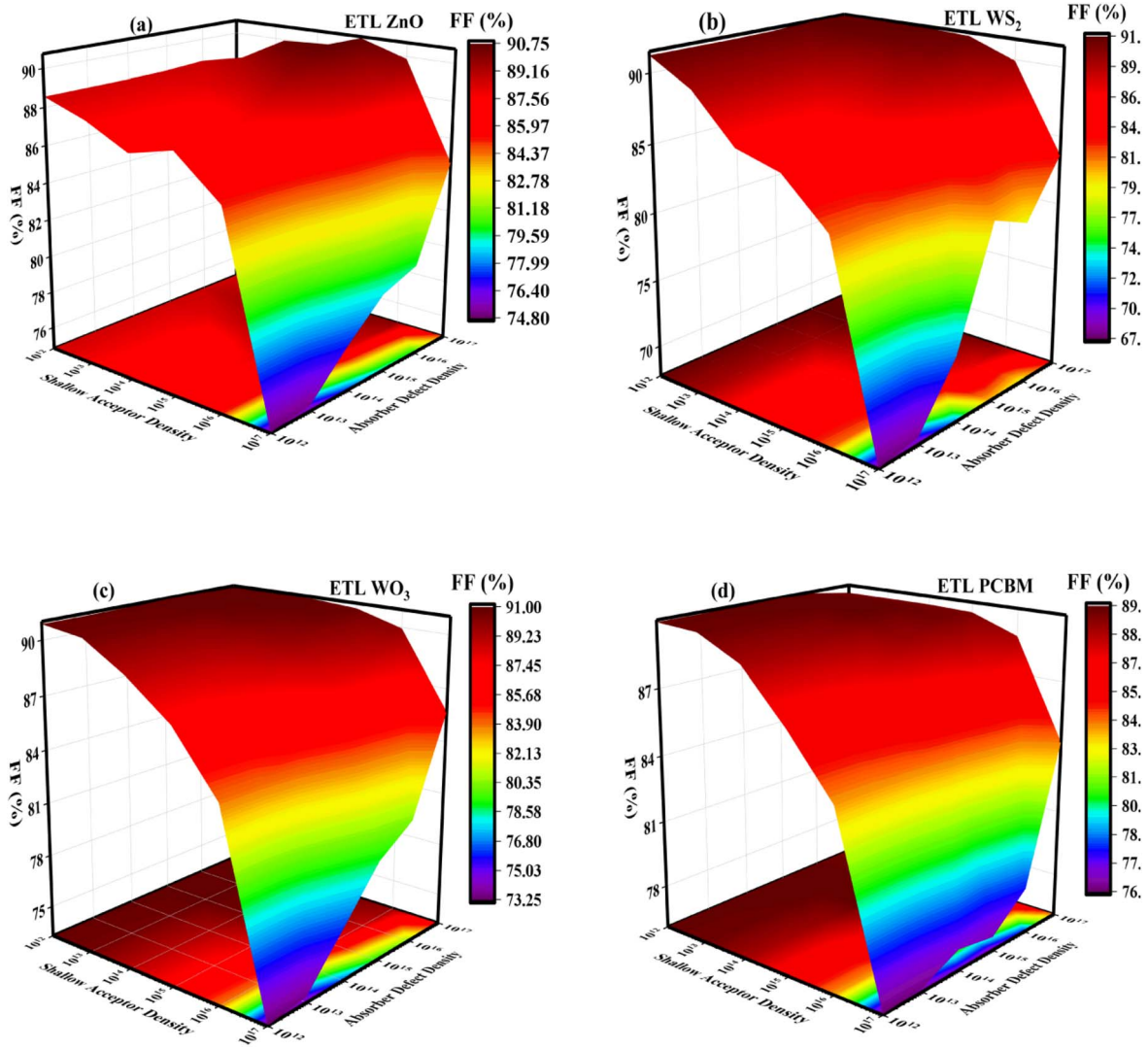

Fig. 16 Three-dimensional surface plot of both fill factor (FF) being a function of shallow acceptor density (N_A) in addition to absorber defect density (N_D) for perovskite solar cells (PSCs) utilizing (a) ZnO, (b) WS_2, (c) WO_3, and (d) PCBM electron transport layers (ETLs).

recombination losses and poor charge extraction when the absorber layer has excessive defects or over-doping, both of which disrupt the optimal electric field and series resistance balance. Notably, the WS_2 and PCBM devices seem to retain slightly higher FF across a broader defect and doping range compared to ZnO and WO_3, suggesting their better resilience against performance degradation. Overall, these plots indicate that while FF is fairly robust under low to moderate absorber imperfections, it degrades significantly when both N_t and N_A exceed critical thresholds, aligning with known recombination and resistive loss mechanisms.

The 3D contour plots in Fig. 17a–d show how the power conversion efficiency (PCE) of perovskite solar cells varies with absorber shallow acceptor density as well as absorber defect density for four different electron transport layers (ETLs): ZnO, WS_2, WO_3, and PCBM. Across all four cases, a clear and consistent trend emerges—as the absorber defect density increases (moving upward in the plots), the PCE decreases sharply, underscoring the critical importance of minimizing defects in the absorber layer to maintain high photovoltaic performance. For ZnO (Fig. 17a), the highest PCE (~29–30%) is observed in a broad region where the shallow acceptor density ranges from approximately 10^{15} to 10^{16} cm^{-3} under low defect densities; however, efficiency deteriorates rapidly as defects rise. WS_2 (Fig. 17b) exhibits the most extensive high-efficiency region (reaching ~30–31%), again centered around a shallow acceptor density of 10^{15}–10^{16} cm^{-3}, suggesting that WS_2 offers slightly better tolerance and potential compared to ZnO. WO_3 (Fig. 17c) shows a narrower optimal region, with maximum PCE (~27–28%) shifting slightly towards higher shallow acceptor densities (around 10^{16} cm^{-3}), while PCBM (Fig. 17d) demonstrates the smallest high-efficiency window and the lowest maximum PCE (~26–27%), indicating it is less effective in this material system.

The results highlight the importance of maintaining low absorber defect density to achieve high power conversion efficiency. Optimizing shallow acceptor density is also critical, with the optimal range varying slightly based on the chosen ETL. Among the materials studied, WS_2 emerged as the most effective ETL, followed by ZnO, while WO_3 and PCBM were less favorable. These insights provide valuable guidance for material selection and device design, emphasizing the strong correlation between absorber quality and ETL compatibility in enhancing perovskite solar cell efficiency.

3.5.6. Effectiveness of HTL alongside absorber thickness. Fig. 18 presents an in-depth analysis of the impact of Rb_2NaInI_6

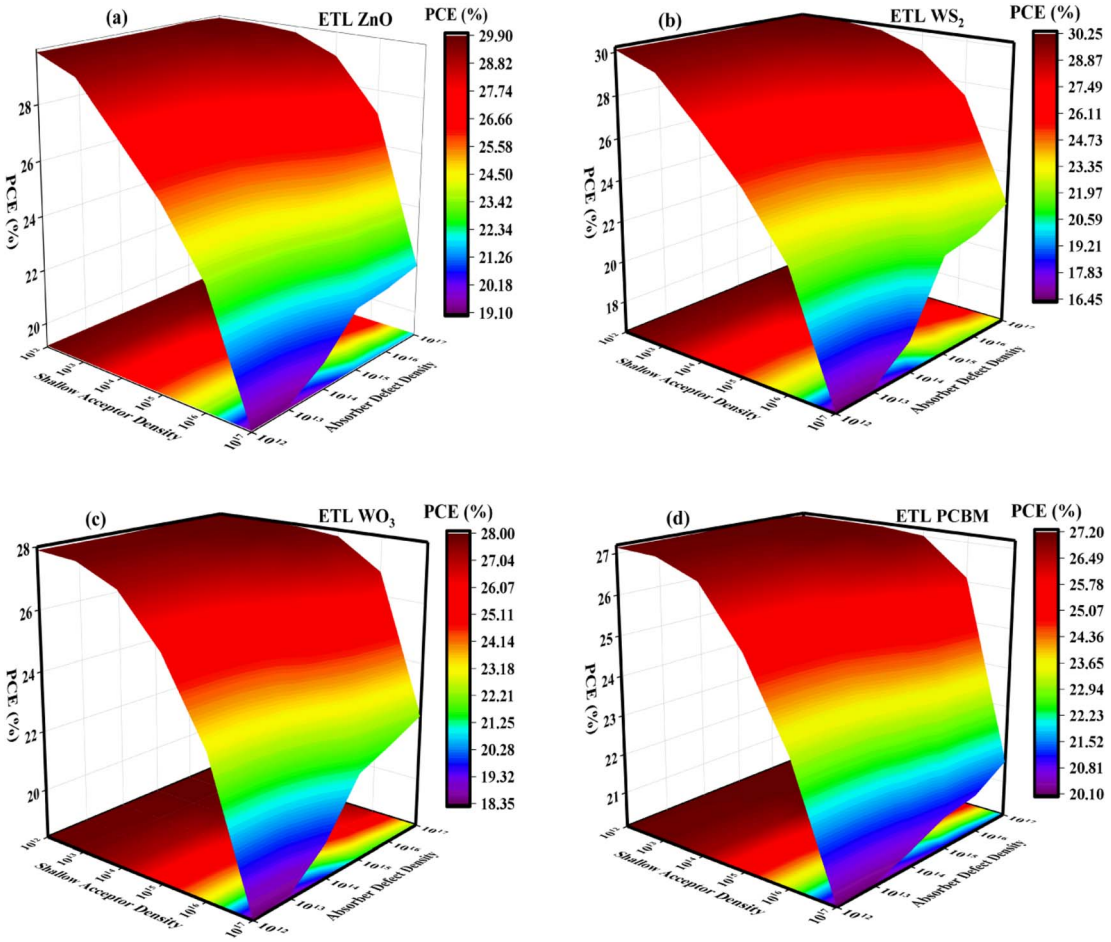

Fig. 17 Three-dimensional surface plot of both power conversion efficiency being a function of shallow acceptor density (N_A) in addition to absorber defect density (N_D) for perovskite solar cells (PSCs) utilizing (a) ZnO, (b) WS_2, (c) WO_3, and (d) PCBM electron transport layers (ETLs).

and CBTS thickness variations on the photovoltaic performance of a solar cell employing different Electron Transport Layers (ETLs): ZnO, WS_2, WO_3, and PCBM. The study evaluates key parameters, including Power Conversion Efficiency (PCE), Fill Factor (FF), Short-circuit Current Density (J_{sc}), and Open-circuit Voltage (V_{oc}), providing valuable insights into absorber and buffer layer optimization for enhanced device performance. Here, the absorber thickness varied from 0.7 to 1.3 μm, while the CBTS thickness varied from 0.1 to 0.6 μm. In Fig. 18a, V_{oc} decreases with increasing Rb_2NaInI_6 absorber thickness, falling from approximately 1.413 V at 0.7 μm to around 1.37 V at 1.2 μm. Among the ETLs, ZnO and WS_2-based devices exhibit better voltage retention, with V_{oc} stabilizing near 1.39 V, while PCBM-based cells show the lowest V_{oc}, indicating greater recombination losses at higher thicknesses due to elongated charge transport paths alternatively, J_{sc} steadily improves as the absorber layer becomes thicker, increasing from about 20.8 mA cm^{-2} to 21.6 mA cm^{-2} across all configurations. This enhancement reflects more effective light harvesting and photocarrier generation with thicker active layers. In terms of fill factor (FF), the values remain relatively stable, fluctuating between 89.0% and 90.5% for ZnO, WS_2, and WO_3-based devices, which indicates minimal impact of absorber thickness on charge extraction efficiency for these ETLs. However, the PCBM-based device displays a slight FF degradation, decreasing from approximately 89.5% to 88%, likely due to increased internal resistive losses. Lastly, the power conversion efficiency (PCE) shows a noticeable enhancement as the Rb_2NaInI_6 thickness increases from 0.7 μm to 1.2 μm, where WS_2-based cells reach up to ~27.0%. At the same time, ZnO-based configurations maintain slightly better overall efficiency, reinforcing ZnO's consistent top performance. Meanwhile, PCBM-based cells exhibit the lowest PCE, affirming their weaker overall performance. The initial increase in PCE is due to enhanced absorption of sunlight and carrier production; however, the enhancement rate diminishes at greater thicknesses, indicating a saturation threshold beyond which further width results in decreasing returns.

In Fig. 18b, V_{oc} remains nearly constant across all CBTS thicknesses (0.1 μm to 0.6 μm), with ZnO and WS_2-based devices maintaining values around 1.398 V, followed by WO_3 at approximately 1.39 V, while PCBM-based cells continue to exhibit the lowest V_{oc} near 1.385 V, confirming the stability of voltage across thicknesses but highlighting PCBM's relatively

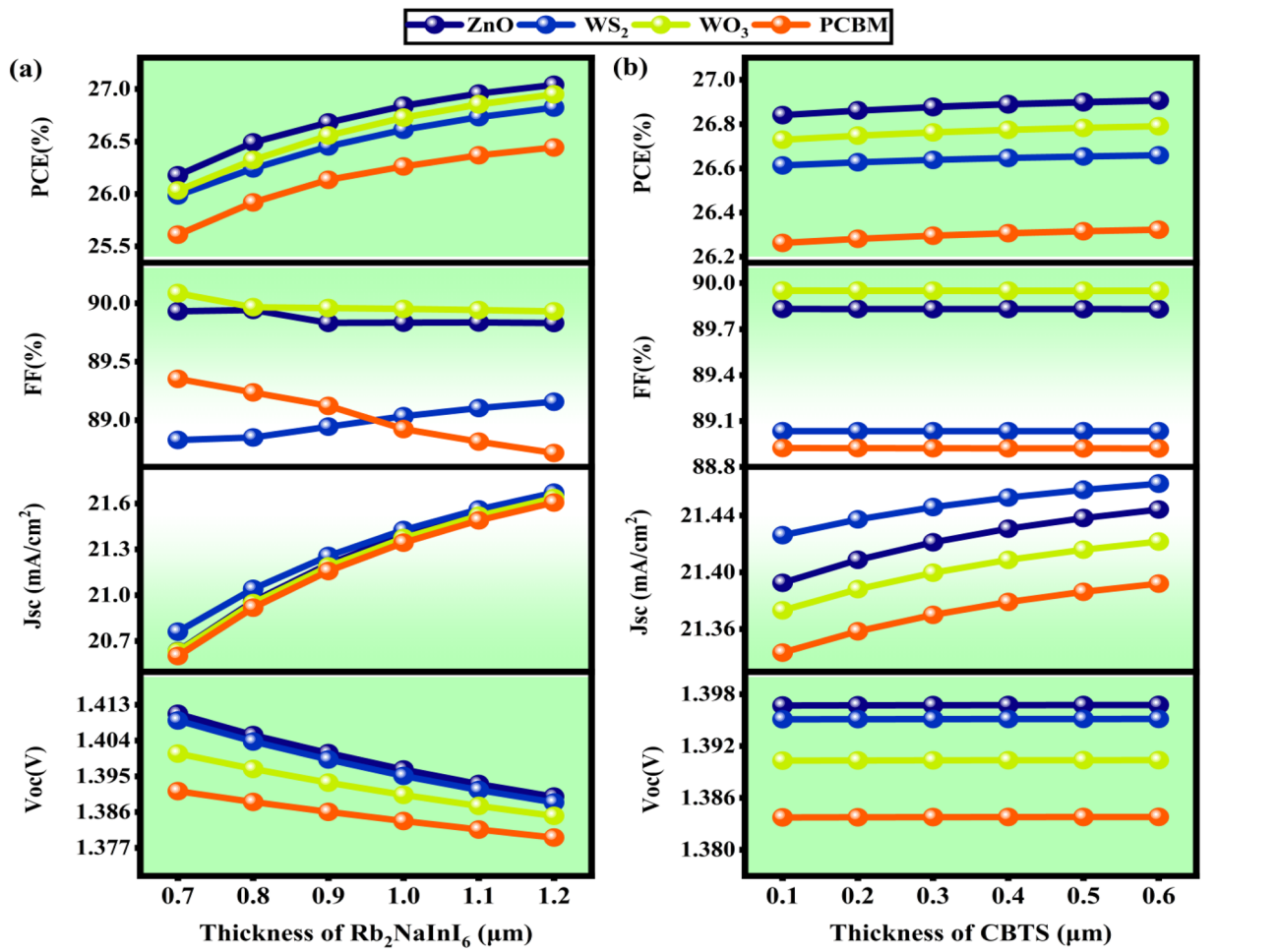

Fig. 18 The influence of modifications in (a) Rb_2NaInI_6 and (b) CBTS thickness demonstrates the effects on V_{oc} (V), J_{sc} (mA cm^{-2}), FF (%), and PCE (%).

weaker performance due to its higher recombination tendency. In contrast, J_{sc} consistently improves with increasing CBTS thickness, rising from ~21.35 mA cm^{-2} at 0.1 μm to ~21.45 mA cm^{-2} at 0.6 μm for WS_2, which outperforms the others, while ZnO and WO_3 show moderate improvements and PCBM lags slightly behind, reinforcing the significance of thicker absorbers in enhancing photocurrent through improved light absorption. Regarding FF, all devices maintain high fill factors ranging from approximately 89.8% to 90.1%, with only slight fluctuations as the CBTS thickness increases, indicating efficient charge transport and minimal resistive losses across all ETLs. Lastly, the PCE increases modestly with CBTS thickness, where ZnO-based devices show the highest performance peaking at ~27.0%, followed by WS_2 (~26.8%), WO_3 (~26.6%), and PCBM (~26.3%). This gradual improvement in efficiency stems from enhanced J_{sc} while V_{oc} and FF remain stable, demonstrating that optimizing CBTS thickness primarily benefits current generation without compromising charge extraction or voltage stability.

3.5.7. Dominance of series (R_s) and shunt (R_{sh}) resistance. Fig. 19 examines the impact of series resistance (R_s) and shunt resistance (R_{sh}) on the photovoltaic performance of a solar cell utilizing different ETLs (ZnO, WS_2, WO_3, and PCBM). The series resistance (R_s) significantly impacts the efficiency of photovoltaic cells. In perovskite solar cells, series resistance arises from the resistance of various layers, including the ETL, HTL, absorber, and both the front and back electrodes.[101] In Fig. 19a, as R_s increases from 1 Ω cm^2 to 6 Ω cm^2, V_{oc} exhibits a slight reduction, with ZnO and WS_2 maintaining the highest values (~1.395 V initially, dropping by ~0.7%), while PCBM shows the lowest V_{oc} (~1.385 V, decreasing by ~0.8%). J_{sc} remains nearly constant across all R_s values, suggesting minimal impact on charge generation. An increase in R_s significantly reduced both FF and PCE, similar to trends in inorganic and organic solar cells.[102] FF declines significantly, with an approximate 6% drop for ZnO and WS_2, while PCBM experiences a steeper decline (~8%). This reduction in FF indicates that an increasing R_s obstructs efficient charge extraction, raising resistive losses. Consequently, PCE follows a similar decreasing trend, with ZnO and WS_2 showing a total drop of ~2%, whereas PCBM undergoes a more significant decrease (~3%), reinforcing that excessive series resistance hinders the overall power conversion

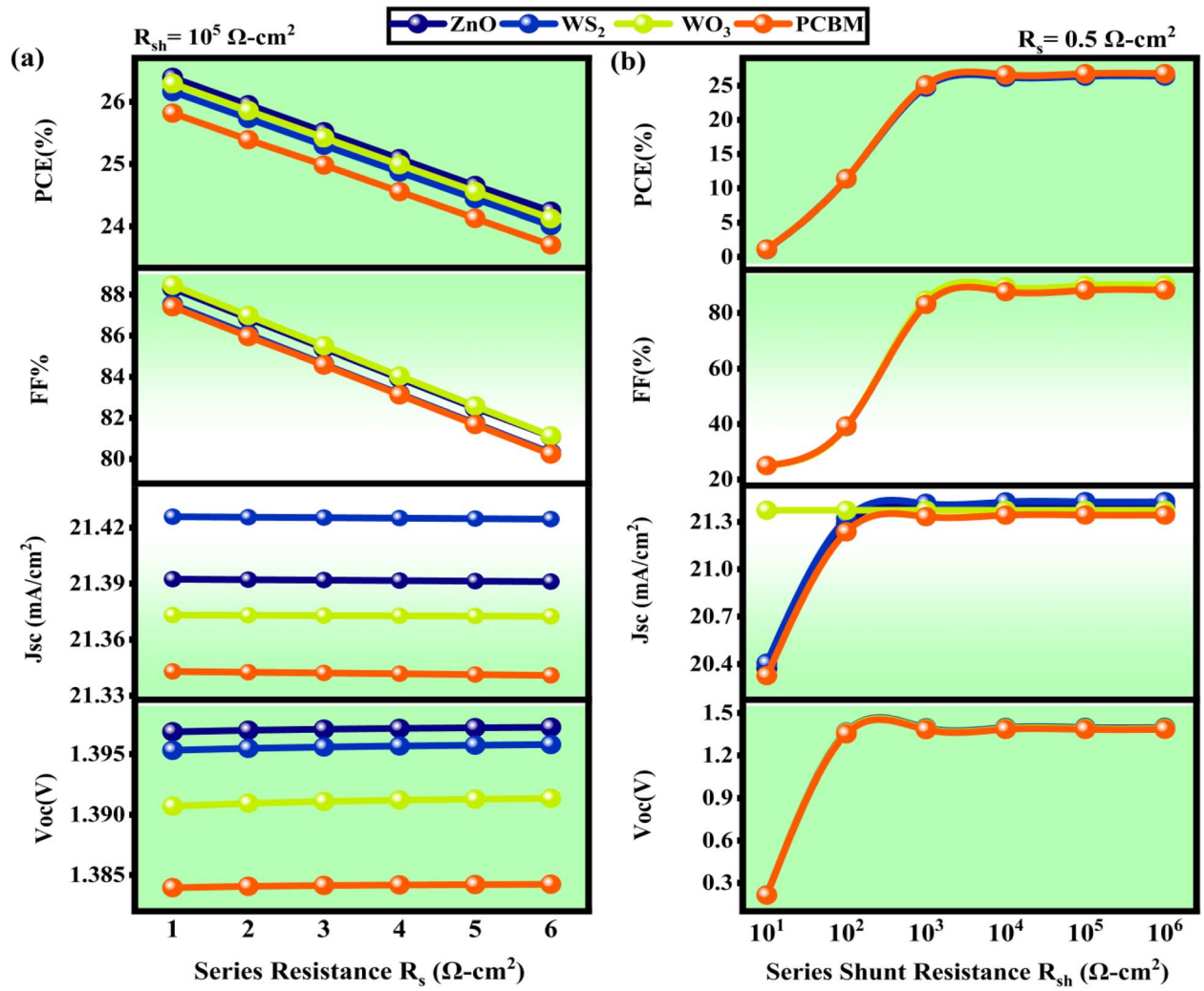

Fig. 19 Effectiveness variations in (a) Shunt resistance (R_s) and (b) series resistance (R_{sh}) both on V_{oc} (V), J_{sc} (mA cm^{-2}), FF (%), and PCE (%).

process. The reduction of FF and PCE with increasing R_s is linked to the rise in power loss.[59] Selecting the minimum R_s helps reduce its impact on PCE and FF, ultimately enhancing solar cell efficiency.

Shunt resistance (R_{sh}) plays an important role in determining the efficiency of photovoltaic cells. Increased R_{sh} often leads to power losses, typically due to issues during manufacturing. Power losses in solar cells are caused by low shunt resistance, as it offers an alternative current path for the light-induced current.[103] In Fig. 19b, as R_{sh} grows from 10 Ω cm^2 to 10^6 Ω cm^2, V_{oc} initially rises sharply from ~0.3 V to ~1.39 V before stabilizing, indicating a significant reduction in leakage currents. J_{sc} exhibits a moderate increase, with ZnO and WS_2 reaching around 21.36 mA cm^{-2}, while PCBM remains slightly lower (~21.30 mA cm^{-2}). FF improves substantially, rising by ~10% for all ETLs as R_{sh} increases, highlighting the suppression of unwanted recombination pathways. As a result, PCE experiences a sharp enhancement, increasing from ~5% to ~25% before stabilizing, emphasizing the crucial role of high R_{sh} in achieving efficient solar cell operation. Among the ETLs, WS_2 consistently performs the best, maintaining superior values in V_{oc}, J_{sc}, FF, and PCE, while PCBM demonstrates the weakest performance across all parameters. These findings confirm that minimizing R_s while maximizing R_{sh} is critical for enhancing device efficiency, with WS_2 emerging as the most promising ETL for stable as well as high-performance solar cell applications. The Shockley equation, outlined in eqn (10) and (11), describes the expected current–voltage (I–V) behaviors of a solar cell under optimal one-sun illumination.[104]

$$J_{SC} = J_{pH} - J_0\left[\exp\left(\frac{q_e(V - JR_s)}{nkT_e}\right) - 1\right] - \frac{V - JR_s}{R_{sh}} \quad (11)$$

$$V_{OC} = \left(\frac{nkT_e}{q_e}\right)\ln\left\{\frac{J_{PH}}{J_0}\left(1 - \frac{V_{OC}}{J_{PH}R_{sh}}\right)\right\} \quad (12)$$

In this case: q_e = elementary charge, J_{PH} = photocurrent density, J_0 = reverse saturation current, n = ideality factor, T_e = 298 K, k = Boltzmann constant. To achieve optimal device performance, it is crucial to avoid localized shunting and current leakage.[105]

3.5.8. Guide on temperature effect on PSCs. As the operating temperature increases from 300 K to 425 K, all four photovoltaic performance parameters—V_{oc}, J_{sc}, FF, and PCE—undergo significant changes, influenced by the choice of electron transport layer (ETL). The impact of temperature on these SCs is shown in Fig. 20a–d. This range was selected to simulate real-world operational conditions, as solar cells often experience elevated temperatures under sunlight. The observed behavior is attributed to temperature-induced changes in material properties – specifically, the reduction in bandgap and increased carrier recombination at higher temperatures, which can affect key performance metrics such as V_{oc} and FF. The

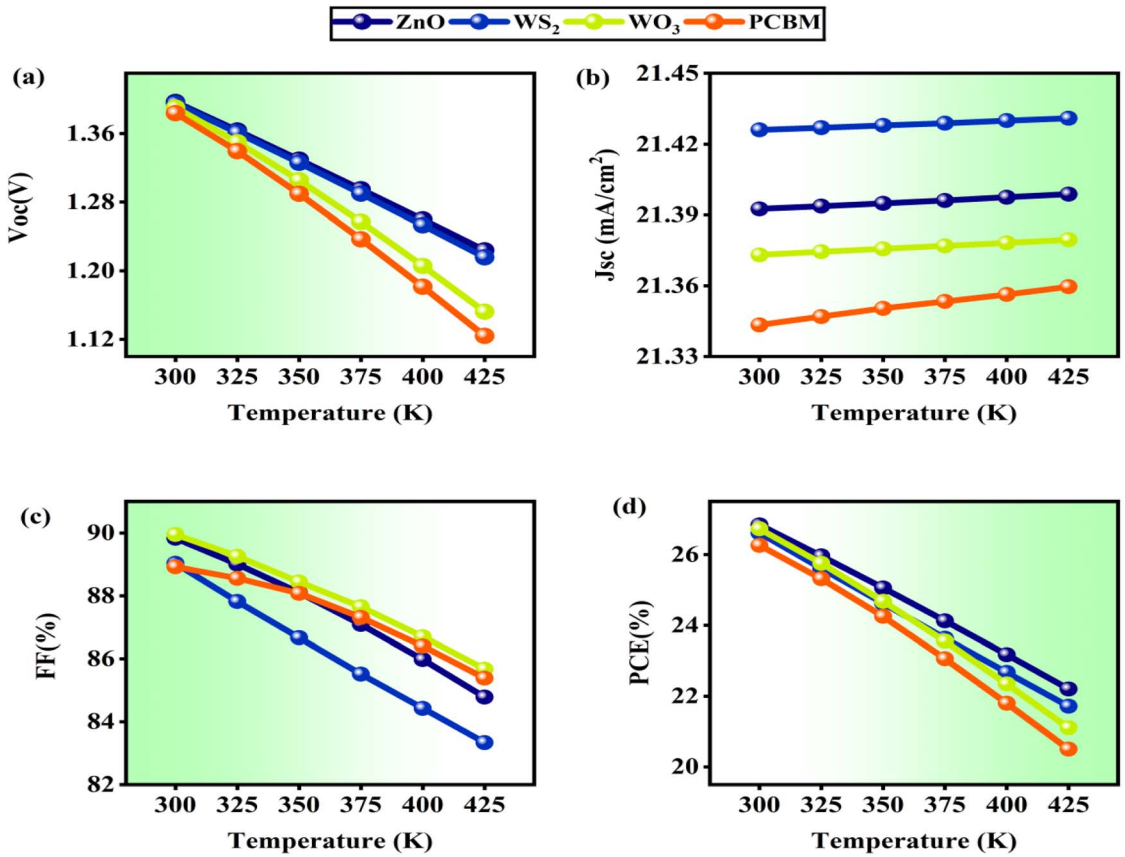

Fig. 20 The temperature variation from 300 K toward 425 K is represented *via* (a) V_{oc} (V), (b) J_{sc} (mA cm^{-2}), (c) FF (%), and (d) PCE (%).

mechanism is primarily related to enhanced phonon interactions, increased intrinsic carrier concentration, and possible interface degradation at elevated temperatures, which collectively influence the device efficiency. This minor improvement in J_{sc} can be attributed to enhanced carrier mobility and reduced recombination resistance at elevated temperatures, though the gain is insufficient to offset the losses in other parameters. The fill factor (FF), which reflects the quality of charge extraction and internal resistive losses, steadily decreases for all devices as temperature rises. ZnO-based solar cells, which begin with a high FF of approximately 90%, drop significantly to around 83%, indicating increased series resistance and reduced diode ideality at higher thermal loads. WS_2, WO_3, and PCBM-based devices also experience FF degradation, though the decline is relatively less severe in PCBM (from ~88% to ~85%), implying a slightly better thermal resilience in charge transport mechanisms. Consequently, the power conversion efficiency (PCE) drops across all ETLs, driven by the combined effect of reduced V_{oc} and FF. ZnO-based solar cells, which initially show the highest PCE of nearly 26% at 300 K, decline to around 22% at 425 K. Similarly, PCBM-based devices drop from ~25.2% to ~21%. Despite ZnO's initial superior performance, it is more susceptible to thermal degradation, especially in FF and V_{oc}, whereas PCBM, though starting with slightly lower values, shows relatively stable thermal behavior. This highlights the importance of selecting ETL materials with better thermal stability to ensure reliable solar cell performance under varying environmental conditions.

3.5.9. Control of capacitance and Mott–Schottky ($1/C^2$). Fig. 21 provides an in-depth analysis of the electrostatic and photophysical parameters for the optimized Rb_2NaInI_6-based solar cells using various ETLs—ZnO, WS_2, WO_3, and PCBM. The Mott–Schottky (M–S) method, based on capacitance–voltage (C–V) analysis, enables the determination of the built-in voltage (V_{bi}) and charge carrier density (N_d). This approach is widely utilized in standard semiconductor devices, particularly those with p–n junctions and semiconductor/metal interfaces containing space charge regions and fixed depletion layers. The junction capacitance for each unit area (C) is calculated using eqn (12).

$$\frac{1}{C^2} = \frac{2\varepsilon_0\varepsilon_r}{qN_d}(V_{bi} - V) \quad (13)$$

In this context, ε_0 is the vacuum permittivity, ε_r is the dielectric constant of the donor material, q represents the electronic charge, and V indicates the applied voltage.[77] In Fig. 21a, the capacitance–voltage (C–V) characteristics reveal an increasing trend with forward bias for all devices, indicating enhanced charge accumulation at higher voltages. Among the ETLs, PCBM-based devices exhibit the highest capacitance, peaking at approximately 10.8 nF cm^{-2} at 0.8 V, while ZnO-based devices show the lowest capacitance, around 8.5 nF cm^{-2}. This suggests a broader depletion width in ZnO, which is beneficial for efficient charge separation and suppression of interface recombination. Fig. 21b displays the Mott–Schottky ($1/C^2 - V$) characteristics. All devices exhibit a typical linear inverse square capacitance profile with increasing voltage. The ZnO-based cell demonstrates the steepest slope, indicating a lower carrier concentration and wider depletion region, which is aligned with its enhanced V_{oc} performance. In contrast, PCBM presents a flatter slope, implying higher doping concentration and possibly inferior junction quality.

3.5.10 Dominance generation and recombination rate. Fig. 21c shows the generation and recombination rates of these four PSCs. As part of the carrier production process, an electron moves from the valence band to the conduction band, leaving behind a hole in the valence band and forming an electron–hole pair.[59] The maximum generation rates for both designs occur at approximately 1.1–1.2 mm, as depicted in Fig. 21c. To calculate $G(x)$, the electron–hole pair production, SCAPS-1D is employed along with the incoming photon flux, Nphot (l, x), as given in eqn (14).

$$G(l, x) = a(l, x).\ \mathrm{Nphot}(l, x) \quad (14)$$

In contrast to the generation process, recombination involves the interaction and separation of electrons and holes within the conduction band. In a solar cell, the recombination rate is influenced by factors such as the density and lifetime of the charge carriers.[106] A decrease in electron–hole recombination is observed due to the presence of defect states in the absorber layer. The formation of energy states within the solar cell impacts the distribution of electron–hole recombination. The recombination rate distribution becomes irregular due to the presence of defects and grain boundaries.[107] The ZnO-based device exhibits the highest generation rate, peaking at approximately 6.9×10^{21} cm^{-3} s^{-1}, followed by WS_2 and PCBM. This superior performance of ZnO highlights its strong ability to support efficient photogeneration under optimized conditions. Fig. 21d depicts the recombination rate across the device thickness. Here, ZnO and WS_2 again outperform PCBM and WO_3, with ZnO-based devices showing a minimal recombination peak of approximately 2.1×10^{19} cm^{-3} s^{-1} near the rear interface, while PCBM-based devices exhibit a significantly higher peak of about 9.5×10^{19} cm^{-3} s^{-1}, indicating greater carrier losses. This stark contrast underscores ZnO's superior passivation capabilities and reduced defect density at interfaces. Overall, ZnO emerges as the most favorable ETL, offering the best balance of low capacitance (indicating wide depletion width), high carrier generation, and minimal recombination. These electrostatic and optical advantages explain the consistently superior device metrics (V_{oc}, J_{sc}, FF, and PCE) observed in earlier figures at optimized absorber and HTL thicknesses.

3.5.11. Power of JV characteristics and QE curve. Fig. 22a and b presents the J–V characteristics and Quantum Efficiency (QE) spectra of FTO/ETL/Rb_2NaInI_6/CBTS-based solar cells using four different Electron Transport Layers (ETLs): ZnO, WS_2, WO_3, and PCBM. The J–V curves show that all configurations—FTO/ZnO/Rb_2NaInI_6/CBTS, FTO/WS_2/Rb_2NaInI_6/CBTS, FTO/WO_3/Rb_2NaInI_6/CBTS, and FTO/PCBM/Rb_2NaInI_6/CBTS—exhibit similar short-circuit current densities (J_{sc}) in the range of approximately 21–22 mA cm^{-2}, indicating efficient light harvesting and comparable photogenerated charge carrier

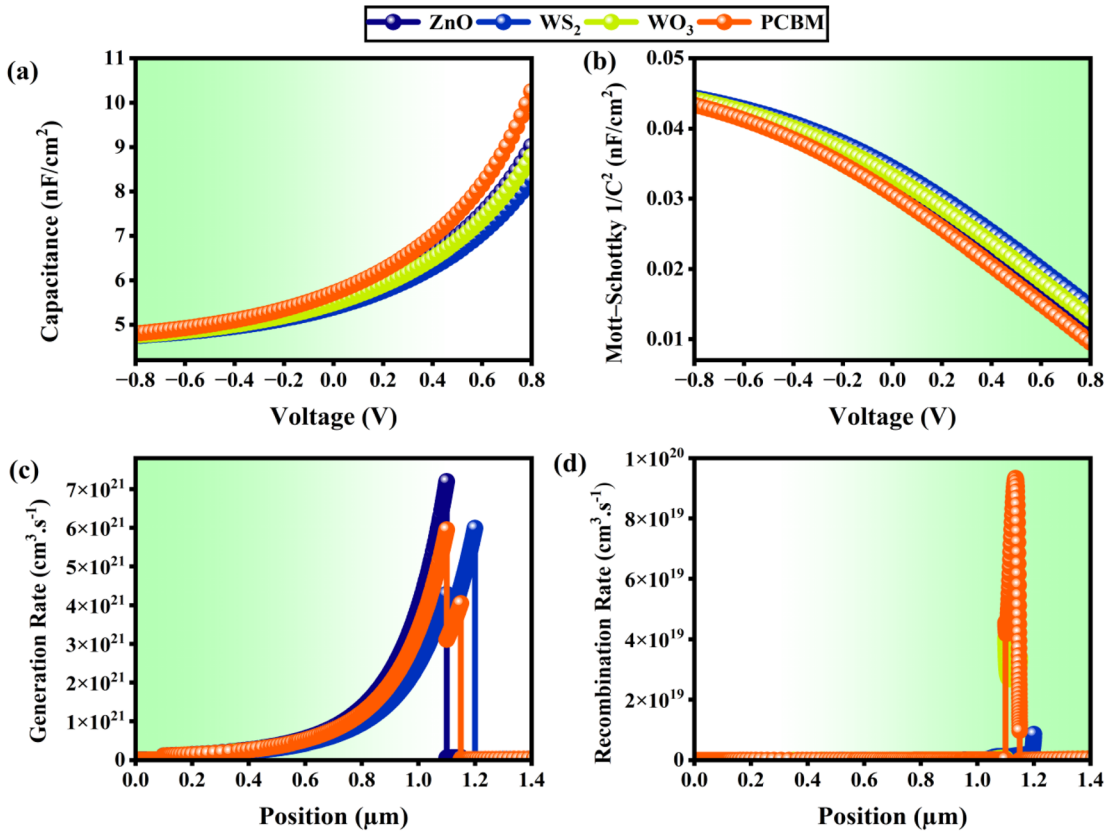

Fig. 21 The improved device's (a) capacitance, (b) Mott–Schottky ($1/C^2$), (c) generation rate, as well as (d) recombination rate.

collection. However, there is a clear variation in open-circuit voltage (V_{oc}), with PCBM yielding the maximum V_{oc} (~1.40 V), followed up WO_3 (~1.39 V), ZnO (~1.38 V), and WS_2 (~1.38 V), demonstrating that the ETL significantly influences the built-in electric field and recombination losses. The fill factor (FF) appears similar across the devices based on the curve shape, suggesting comparable series and shunt resistance characteristics. While PCE is not plotted directly, it is inferred that FTO/

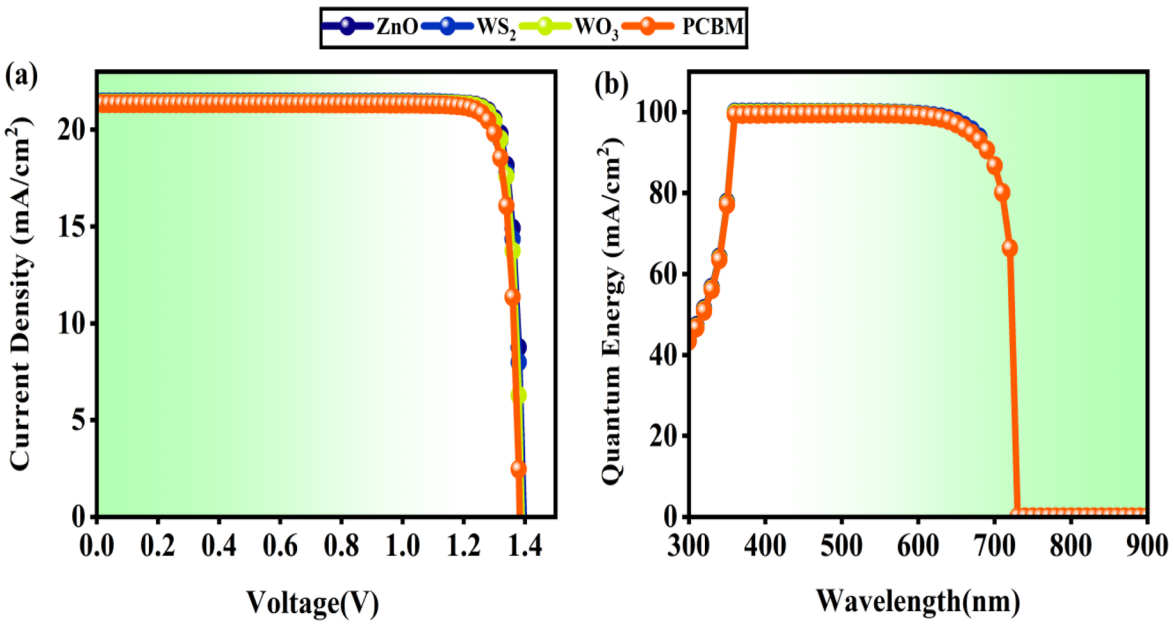

Fig. 22 The (a) J–V characteristics as well as (b) QE curve of the twin PSCs.

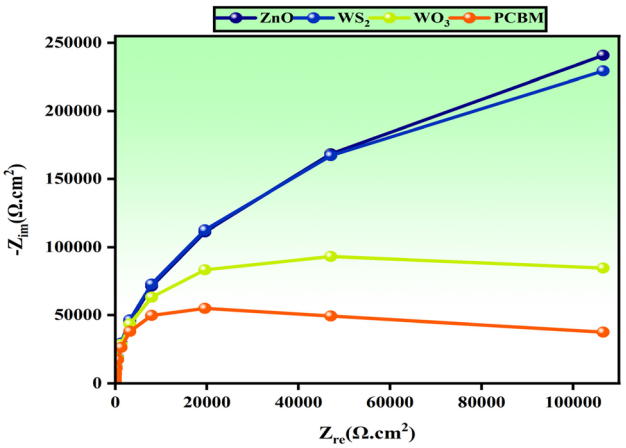

Fig. 23 Nyquist plot of the diverse HTL materials derived from the construction using the absorber Rb_2NaInI_6.

PCBM/Rb_2NaInI_6/CBTS and FTO/WO_3/Rb_2NaInI_6/CBTS structures would exhibit higher efficiencies due to their superior V_{oc}. The QE spectra further reinforce these observations, showing nearly identical spectral responses across all devices with high quantum efficiencies (~100%) in the visible range (400–700 nm) and a sharp cutoff near 720 nm, indicating the absorber's bandgap limit. These similar QE responses confirm that the absorber, Rb_2NaInI_6, governs the light absorption and charge generation, while the ETL predominantly impacts charge transport and extraction, particularly influencing V_{oc}. Overall, the findings underscore that while J_{sc} and QE remain largely unaffected by the ETL type, PCBM and WO_3 offer superior V_{oc} performance, making them the most favorable ETL candidates in this device configuration for enhanced power conversion efficiency.

3.5.12. Nyquist plot analysis. Fig. 23 presents the Nyquist plot derived from electrochemical impedance spectroscopy (EIS) to compare the interfacial characteristics of various electron transport layer (ETL) materials-ZnO, WS_2, WO_3, and PCBM-used in Rb_2NaInI_6-based perovskite solar cells. The plot displays the imaginary component of impedance ($-Z_{im}$) *versus* the real component (Z_{re}), allowing a clear visualization of charge transport resistance and recombination behavior. Among the materials studied, ZnO and WS_2 exhibit the largest semicircular arcs, with ZnO reaching a peak-Z_{im} of approximately 240 000 Ω cm^2, indicating higher interfacial resistance and lower charge recombination rates. This behavior is attributed to their wide bandgaps, favorable conduction band alignment, and superior electron mobility, which collectively enhance their charge-blocking capability and minimize leakage current.[108,109] On the other hand, WO_3 and PCBM show significantly smaller arc diameters, peaking below 100 000 Ω cm^2, which suggests faster charge transfer kinetics but possibly at the expense of increased recombination losses.[110] The pronounced impedance of ZnO and WS_2 is indicative of their strong recombination suppression abilities and higher series resistance, which may translate into higher open-circuit voltage (V_{oc}) and device stability.[108] Although PCBM remains a widely adopted ETL for its excellent electronic properties and compatibility, its lower impedance values may correspond to limited recombination control in this specific device architecture.[110]

3.6. Comparative evaluation with previous works

Table 3 compares previously reported photovoltaic device structures and the optimized configurations proposed in this work. The comparative performance evaluation of the proposed device architectures based on the Rb_2NaInI_6 absorber layer demonstrates a remarkable advancement over previously reported structures. As shown in the table, prior studies employing various absorbers such as Cs_2BiAgI_6, $MAPbI_3$, $Cs_2CuBiBr_6$, and $Cs_2AgBiBr_6$ paired with different ETL/HTL combinations exhibited power conversion efficiencies (PCE) ranging from 16.23% to 23.05%. Among these, the structure ITO/TiO_2/CCSCNCs/Cu_2O/Pt reported the highest efficiency (23.05%) with

Table 3 Comparative evaluation of the performance of diverse photovoltaic cell architectures with varied absorber and ETL/HTL the layout

Structure	V_{oc} (V)	J_{sc} (mA cm^{-2})	FF (%)	PCE (%)	Ref.
FTO/TiO_2/$Cs_2AgBiBr_6$/spiro-OMeTAD/Au	1.511	3.89	51.76	3.04	52
ITO/SnO_2/$Cs_2AgBiBr_6$/spiro-OMeTAD/Au	0.92	11.4	60.93	6.37	54
Glass/FTO/TiO_2/$Cs_2AgBiBr_6$/Cu_2O/Au	1.5	11.45	42.1	7.25	56
FTO/TiO_2/$Cs_2AgSbBr_6$/spiro-OMeTAD/Ag	0.94	22.49	50.2	10.69	111
FTO/Ws_2/$Cs_2CuBiBr_6$/spiro-OMeTAD/Ag	0.60	34.59	67.36	14.08	111
Ohmic contact/spiro-OMeTAD/Cs_2BiAgI_6/TiO_2/SnO_2: F(ZnO_2)/ohmic contact	1.18	16.2	80.20	15.90	112
FTO/PCBM/Cs_2BiAgI_6/PTAA/Pt	1.08	19.94	74.87	16.23	113
ITO/WO_3/$MAPbI_3$/Mg-$CuCrO_2$/Pt	0.89	23.24	83.95	17.53	114
ITO/WS_2/$Cs_2CuBiBr_6$/CBTS/Ni	0.71	35.63	77.57	19.70	115
ITO/TiO_2/Cs_2BiAgI_6/CBTS/Pt	1.08	23.80	83.61	21.55	116
FTO/TiO_2/CCSCNCs/Cu_2O/Pt	1.30	21.35	83.02	23.07	117
FTO/AZnO/$Cs_2AgBiBr_6$/CNTS/Pt	1.37	21.38	79.93	23.50	118
ITO/WS_2/Cs_2KIrCl_6/V_2O_5	1.52	14.809	85.12	19.18	119
ITO/ZnO/Cs_2KIrCl_6/V_2O_5	1.54	15.479	89.32	21.30	119
FTO/PCBM/Rb_2NaInI_6/CBTS/Pt	1.38	21.34	88.92	26.26	This work
FTO/WS_2/Rb_2NaInI_6/CBTS/Pt	1.39	21.42	89.03	26.61	This work
FTO/WO_3/Rb_2NaInI_6/CBTS/Pt	1.39	21.37	88.95	26.73	This work
FTO/ZnO/Rb_2NaInI_6/CBTS/Pt	1.39	21.39	89.83	26.84	This work

a short-circuit current density (J_{sc}) of 25.83 mA cm^{-2} and a fill factor (FF) of 82.44%. In contrast, the present work introduces novel FTO-based configurations with Rb_2NaInI_6 as the absorber and CBTS/Pt as the back contact, integrated with varying ETL materials (PCBM, WS_2, WO_3, and ZnO). These optimized designs achieved open-circuit voltages (V_{oc}) up to 1.39 V, J_{sc} values up to 21.39 mA cm^{-2}, and FF exceeding 89%, resulting in an impressive peak PCE of 26.84%. Notably, the configuration FTO/ZnO/Rb_2NaInI_6/CBTS/Pt delivered the best performance (V_{oc} = 1.39 V, J_{sc} = 21.39 mA cm^{-2}, FF = 89.83%, PCE = 26.84%), significantly outperforming all previously reported structures. This enhancement is attributed to the superior band alignment, minimal recombination losses, and improved charge extraction at the interfaces facilitated by the optimized Rb_2NaInI_6 absorber and ZnO ETL. Thus, this work highlights the potential of lead-free, double perovskite-based solar cells in achieving high efficiency while maintaining environmental stability and reduced toxicity, thereby paving the way for scalable and sustainable photovoltaic technologies.

4. Conclusion

In this study, a comprehensive investigation into the potential of the lead-free double perovskite Rb_2NaInI_6 was carried out using a dual approach involving first-principles Density Functional Theory (DFT) calculations and one-dimensional solar cell simulation *via* SCAPS-1D. The DFT analysis confirmed that Rb_2NaInI_6 crystallizes in a stable cubic $Fm\bar{3}m$ phase, exhibiting a moderate bandgap of 0.73 eV (*via* GGA functional) and 1.70 eV (*via* TB-mBj functional), which, along with strong In-5s and I-5p hybridization in the density of states, ensures favorable charge transport characteristics. The material also demonstrated high absorption coefficients in the visible to ultraviolet (UV) range-peaking around 12 eV-low reflectivity (<30%), and a high dielectric constant, all of which suggest its promise for efficient light harvesting and minimal optical loss in photovoltaic and optoelectronic applications. On the simulation side, SCAPS-1D modeling complemented the theoretical predictions by revealing a wider effective indirect bandgap of 1.702 eV, optimal for solar absorption. Charge distribution analysis highlighted sodium atoms as dominant carriers, with strong covalent In–I bonds and ionic Rb–I/Na–I interactions contributing to the overall material stability. Among 36 device configurations studied using six different ETL and HTL combinations, CBTS emerged as the best-performing HTL when coupled with ZnO as the ETL. The structure FTO/ZnO/Rb_2NaInI_6/CBTS/Pt achieved a peak PCE of 26.84%, slightly surpassing the WO_3-based counterpart. It was also observed that increasing the absorber thickness significantly enhanced performance, whereas ETL thickness had a negligible impact. The simulation further validated device robustness through Nyquist plots, *J–V*, and QE curves under various operating conditions, including thermal variation and defect-induced recombination. These results affirm the viability of Rb_2NaInI_6 as a lead-free and environmentally benign material and underscore its capability to deliver high photovoltaic efficiency in tandem solar architectures. This combined theoretical–simulation approach confirms Rb_2NaInI_6 as a strong candidate for high-efficiency, environmentally friendly, lead-free perovskite solar cells, offering a promising pathway toward sustainable and scalable photovoltaic technologies.

Author contributions

Akram Hossan Mahedi: investigation, methodology, data curation, conceptualization, writing original manuscript; Salah Uddin: investigation, methodology, data curation, review-editing; Mohammad Yasin Hayat Khan: formal analysis, software, methodology, review-editing; Md. Tarekuzzaman: formal analysis, software, conceptualization, review-editing; O. Alsalmi: formal analysis, methodology, data curation, review-editing; Md. Rasheduzzaman: formal analysis, validation, review-editing; S. M. G Mostafa: formal analysis, data curation, review-editing, M. Moazzam Hossen: formal analysis, data curation, review-editing, Md. Zahid Hasan: formal analysis, validation, supervision, review-editing.

Conflicts of interest

There is no conflict to declare.

Data availability

Data will be made available on request.

Acknowledgements

The authors extend their appreciation to Umm Al-Qura University, Saudi Arabia for funding this research work through grant number: 25UQU4300099GSSR11.

References

1 N.-G. Park, M. Grätzel, T. Miyasaka, K. Zhu and K. Emery, *Nat. Energy*, 2016, **1**, 16152.
2 J. Allison, *JOM*, 2011, **63**, 15–18.
3 R. Dehghannasiri, D. Xue, P. V. Balachandran, M. R. Yousefi, L. A. Dalton, T. Lookman and E. R. Dougherty, *Comput. Mater. Sci.*, 2017, **129**, 311–322.
4 K. I. Ramachandran, D. Gopakumar and K. Namboori, *Computational Chemistry and Molecular Modeling*, Springer Berlin Heidelberg, Berlin, Heidelberg, 2008.
5 P. Geerlings, E. Chamorro, P. K. Chattaraj, F. De Proft, J. L. Gázquez, S. Liu, C. Morell, A. Toro-Labbé, A. Vela and P. Ayers, *Theor. Chem. Acc.*, 2020, **139**, 36.
6 G. R. Schleder, A. Fazzio and J. T. Arantes, *J. Comput. Chem.*, 2017, **38**, 2675–2679.
7 B. Hammer and J. K. Nørskov, in *Advances in Catalysis*, Elsevier, 2000, vol. 45, pp. 71–129.
8 C. Freysoldt, B. Grabowski, T. Hickel, J. Neugebauer, G. Kresse, A. Janotti and C. G. Van De Walle, *Rev. Mod. Phys.*, 2014, **86**, 253–305.
9 G. R. Schleder, A. Fazzio and J. T. Arantes, *Int. J. Quantum Chem.*, 2019, **119**, e25874.

10 A. S. Barnard, *Rep. Prog. Phys.*, 2010, **73**, 086502.
11 F. Baletto and R. Ferrando, *Rev. Mod. Phys.*, 2005, **77**, 371–423.
12 J. E. Padilha, A. Fazzio and A. J. R. Da Silva, *Phys. Rev. Lett.*, 2015, **114**, 066803.
13 T. B. Martins, R. H. Miwa, A. J. R. Da Silva and A. Fazzio, *Phys. Rev. Lett.*, 2007, **98**, 196803.
14 F. H. Tian and C. B. Liu, *J. Phys. Chem. B*, 2006, **110**, 17866–17871.
15 J. K. Nørskov, T. Bligaard, J. Rossmeisl and C. H. Christensen, *Nat. Chem.*, 2009, **1**, 37–46.
16 G. R. Schleder, A. C. M. Padilha, C. M. Acosta, M. Costa and A. Fazzio, *J. Phys. Mater.*, 2019, **2**, 032001.
17 L. Zheng, A. Nozariasbmarz, Y. Hou, J. Yoon, W. Li, Y. Zhang, H. Wu, D. Yang, T. Ye, M. Sanghadasa, K. Wang, B. Poudel, S. Priya and K. Wang, *Nat. Commun.*, 2022, **13**, 7399.
18 T. M. Brenner, D. A. Egger, L. Kronik, G. Hodes and D. Cahen, *Nat. Rev. Mater.*, 2016, **1**, 15007.
19 S. De Wolf, J. Holovsky, S.-J. Moon, P. Löper, B. Niesen, M. Ledinsky, F.-J. Haug, J.-H. Yum and C. Ballif, *J. Phys. Chem. Lett.*, 2014, **5**, 1035–1039.
20 L. Yue, B. Yan, M. Attridge and Z. Wang, *Sol. Energy*, 2016, **124**, 143–152.
21 L. M. Herz, *ACS Energy Lett.*, 2017, **2**, 1539–1548.
22 S. D. Stranks, G. E. Eperon, G. Grancini, C. Menelaou, M. J. P. Alcocer, T. Leijtens, L. M. Herz, A. Petrozza and H. J. Snaith, *Science*, 2013, **342**, 341–344.
23 C. Wehrenfennig, G. E. Eperon, M. B. Johnston, H. J. Snaith and L. M. Herz, *Adv. Mater.*, 2014, **26**, 1584–1589.
24 Y. Zhou, J. Chen, O. M. Bakr and O. F. Mohammed, *ACS Energy Lett.*, 2021, **6**, 739–768.
25 X. Hu, X. Zhang, L. Liang, J. Bao, S. Li, W. Yang and Y. Xie, *Adv. Funct. Mater.*, 2014, **24**, 7373–7380.
26 J. D. Majher, M. B. Gray, T. A. Strom and P. M. Woodward, *Chem. Mater.*, 2019, **31**, 1738–1744.
27 R. A. John, N. Shah, S. K. Vishwanath, S. E. Ng, B. Febriansyah, M. Jagadeeswararao, C.-H. Chang, A. Basu and N. Mathews, *Nat. Commun.*, 2021, **12**, 3681.
28 A. Kojima, K. Teshima, Y. Shirai and T. Miyasaka, *J. Am. Chem. Soc.*, 2009, **131**, 6050–6051.
29 H. Min, D. Y. Lee, J. Kim, G. Kim, K. S. Lee, J. Kim, M. J. Paik, Y. K. Kim, K. S. Kim, M. G. Kim, T. J. Shin and S. Il Seok, *Nature*, 2021, **598**, 444–450.
30 B. Park and S. I. Seok, *Adv. Mater.*, 2019, **31**, 1805337.
31 T. A. Berhe, W.-N. Su, C.-H. Chen, C.-J. Pan, J.-H. Cheng, H.-M. Chen, M.-C. Tsai, L.-Y. Chen, A. A. Dubale and B.-J. Hwang, *Energy Environ. Sci.*, 2016, **9**, 323–356.
32 M. Saliba, T. Matsui, K. Domanski, J.-Y. Seo, A. Ummadisingu, S. M. Zakeeruddin, J.-P. Correa-Baena, W. R. Tress, A. Abate, A. Hagfeldt and M. Grätzel, *Science*, 2016, **354**, 206–209.
33 J. K. Nam, D. H. Chun, R. J. K. Rhee, J. H. Lee and J. H. Park, *Adv. Sci.*, 2018, **5**, 1800509.
34 F. Ünlü, E. Jung, J. Haddad, A. Kulkarni, S. Öz, H. Choi, T. Fischer, S. Chakraborty, T. Kirchartz and S. Mathur, *APL Mater.*, 2020, **8**, 070901.
35 M. Wang, W. Wang, B. Ma, W. Shen, L. Liu, K. Cao, S. Chen and W. Huang, *Nano-Micro Lett.*, 2021, **13**, 62.
36 M. Zhang, Z. Zhang, H. Cao, T. Zhang, H. Yu, J. Du, Y. Shen, X.-L. Zhang, J. Zhu, P. Chen and M. Wang, *Mater. Today Energy*, 2022, **23**, 100891.
37 S. Ghosh, H. Shankar and P. Kar, *Mater. Adv.*, 2022, **3**, 3742–3765.
38 D. Yang, J. Lv, X. Zhao, Q. Xu, Y. Fu, Y. Zhan, A. Zunger and L. Zhang, *Chem. Mater.*, 2017, **29**, 524–538.
39 S. Shao, J. Liu, G. Portale, H. Fang, G. R. Blake, G. H. Ten Brink, L. J. A. Koster and M. A. Loi, *Adv. Energy Mater.*, 2018, **8**, 1702019.
40 F. Hao, C. C. Stoumpos, D. H. Cao, R. P. H. Chang and M. G. Kanatzidis, *Nat. Photonics*, 2014, **8**, 489–494.
41 H. Sabbah and Z. A. Baki, *Nanomaterials*, 2023, **13**, 1537.
42 G. Nasti and A. Abate, *Adv. Energy Mater.*, 2020, **10**, 1902467.
43 J. Tong, J. Gong, M. Hu, S. K. Yadavalli, Z. Dai, F. Zhang, C. Xiao, J. Hao, M. Yang, M. A. Anderson, E. L. Ratcliff, J. J. Berry, N. P. Padture, Y. Zhou and K. Zhu, *Matter*, 2021, **4**, 1365–1376.
44 C. C. Stoumpos, C. D. Malliakas and M. G. Kanatzidis, *Inorg. Chem.*, 2013, **52**, 9019–9038.
45 S. Rühle, *Sol. Energy*, 2016, **130**, 139–147.
46 C. Wang, Y. Zhang, F. Gu, Z. Zhao, H. Li, H. Jiang, Z. Bian and Z. Liu, *Matter*, 2021, **4**, 709–721.
47 J. Arayro, R. Mezher and H. Sabbah, *Coatings*, 2023, **13**, 1258.
48 P.-K. Kung, M.-H. Li, P.-Y. Lin, J.-Y. Jhang, M. Pantaler, D. C. Lupascu, G. Grancini and P. Chen, *Sol. RRL*, 2020, **4**, 1900306.
49 F. Giustino and H. J. Snaith, *ACS Energy Lett.*, 2016, **1**, 1233–1240.
50 A. Raj, M. Kumar, A. Kumar, A. Laref, K. Singh, S. Sharma and A. Anshul, *Mater. Lett.*, 2022, **313**, 131692.
51 S. R. Hosseini, M. Bahramgour, P. Yardani Sefidi, A. Tabatabaei Mashayekh, A. Moradi, N. Delibas, M. G. Hosseini and A. Niaei, *Heliyon*, 2022, **8**, e11471.
52 E. Greul, M. L. Petrus, A. Binek, P. Docampo and T. Bein, *J. Mater. Chem. A*, 2017, **5**, 19972–19981.
53 F. Igbari, R. Wang, Z.-K. Wang, X.-J. Ma, Q. Wang, K.-L. Wang, Y. Zhang, L.-S. Liao and Y. Yang, *Nano Lett.*, 2019, **19**, 2066–2073.
54 Z. Zhang, Q. Sun, Y. Lu, F. Lu, X. Mu, S.-H. Wei and M. Sui, *Nat. Commun.*, 2022, **13**, 3397.
55 T. I. Alanazi, *Crystals*, 2023, **13**, 267.
56 M. T. Islam, M. R. Jani, S. M. Al Amin, M. S. U. Sami, K. M. Shorowordi, M. I. Hossain, M. Devgun, S. Chowdhury, S. Banerje and S. Ahmed, *Opt. Mater.*, 2020, **105**, 109957.
57 I. Chabri, Y. Benhouria, A. Oubelkacem, A. Kaiba, I. Essaoudi and A. Ainane, *Optik*, 2023, **274**, 170560.
58 H. I. Alkhammash, M. Mottakin, M. M. Hossen, M. Akhtaruzzaman and M. J. Rashid, *Semicond. Sci. Technol.*, 2023, **38**, 015005.
59 M. K. Hossain, M. H. K. Rubel, G. F. I. Toki, I. Alam, Md. F. Rahman and H. Bencherif, *ACS Omega*, 2022, **7**, 43210–43230.

60 M. K. Hossain, M. S. Uddin, G. F. I. Toki, M. K. A. Mohammed, R. Pandey, J. Madan, Md. F. Rahman, Md. R. Islam, S. Bhattarai, H. Bencherif, D. P. Samajdar, M. Amami and D. K. Dwivedi, *RSC Adv.*, 2023, **13**, 23514–23537.
61 M. I. Kholil, M. T. H. Bhuiyan, M. A. Rahman, M. S. Ali and M. Aftabuzzaman, *AIP Adv.*, 2021, **11**, 035229.
62 E. T. McClure, M. R. Ball, W. Windl and P. M. Woodward, *Chem. Mater.*, 2016, **28**, 1348–1354.
63 H. Lei, D. Hardy and F. Gao, *Adv. Funct. Mater.*, 2021, **31**, 2105898.
64 F. Paquin, J. Rivnay, A. Salleo, N. Stingelin and C. Silva, *arXiv*, 2015, preprint, arXiv:1310.8002, DOI: **10.48550/ARXIV.1310.8002**.
65 K. Schwarz, *J. Solid State Chem.*, 2003, **176**, 319–328.
66 J. P. Perdew, K. Burke and M. Ernzerhof, *Phys. Rev. Lett.*, 1996, **77**, 3865–3868.
67 H. Jiang, *J. Chem. Phys.*, 2013, **138**, 134115.
68 M. D. Segall, P. J. D. Lindan, M. J. Probert, C. J. Pickard, P. J. Hasnip, S. J. Clark and M. C. Payne, *J. Phys. Condens. Matter*, 2002, **14**, 2717–2744.
69 S. Uddin, A. Das, M. A. Rayhan, S. Ahmad, R. M. Khokan, Md. Rasheduzzaman, R. Das, A. Ullah, Y. Arafat and Md. Z. Hasan, *J. Comput. Electron.*, 2024, **23**, 1217–1237.
70 M. A. Hadi, R. V. Vovk and A. Chroneos, *J. Mater. Sci. Mater. Electron.*, 2016, **27**, 11925–11933.
71 A. K Al-Mousoi, M. K. A. Mohammed, S. Q. Salih, R. Pandey, J. Madan, D. Dastan, E. Akman, A. A. Alsewari and Z. M. Yaseen, *Energy Fuels*, 2022, **36**, 14403–14410.
72 R. A. Jabr, M. Hamad and Y. M. Mohanna, *Int. J. Electr. Eng. Educ.*, 2007, **44**, 23–33.
73 Md. Hasan Ali, A. T. M. Saiful Islam, M. D. Haque, Md. Ferdous Rahman, M. Khalid Hossain, N. Sultana and A. Z. M. Touhidul Islam, *Mater. Today Commun.*, 2023, **34**, 105387.
74 A. K. Al-Mousoi, M. K. A. Mohammed, R. Pandey, J. Madan, D. Dastan, G. Ravi, P. Sakthivel and G. Anandha Babu, *RSC Adv.*, 2022, **12**, 32365–32373.
75 M. K. Hossain, M. H. K. Rubel, G. F. I. Toki, I. Alam, Md. F. Rahman and H. Bencherif, *ACS Omega*, 2022, **7**, 43210–43230.
76 Md. A. Rahman, Md. Z. Rahaman and Md. A. Rahman, *Int. J. Mod. Phys. B*, 2016, **30**, 1650199.
77 S. Karthick, S. Velumani and J. Bouclé, *Opt. Mater.*, 2022, **126**, 112250.
78 Naureen, Sadanand, S. Rai, R. K. Yadav, P. Lohia and D. K. Dwivedi, *Opt. Quantum Electron.*, 2023, **55**(6), 541.
79 Y. Pan and F. Yang, *J. Mater. Res. Technol.*, 2024, **28**, 381–389.
80 K. M. Hossain, Md. Zahid Hasan and Md. Lokman Ali, *Results Phys.*, 2020, **19**, 103337.
81 S. J. Mole, X. Zhou and R. Liu, *J. Phys. Chem.*, 1996, **100**, 14665–14671.
82 S. Al-Qaisi, N. Iram, A. Boutramine, A. K. Alqorashi, T. A. Alrebdi, H. Rached, M. Ezzeldien, A. S. Verma, N. Rahman and Md. F. Rahman, *J. Inorg. Organomet. Polym. Mater.*, 2024, **34**, 6146–6158.
83 N. A. Noor, M. W. Iqbal, T. Zelai, A. Mahmood, H. M. Shaikh, S. M. Ramay and W. Al-Masry, *J. Mater. Res. Technol.*, 2021, **13**, 2491–2500.
84 M. Kibbou, Z. Haman, I. Essaoudi and A. Ainane, *J. Solid State Chem.*, 2023, **317**, 123698.
85 A. M. Smith and S. Nie, *Acc. Chem. Res.*, 2010, **43**, 190–200.
86 Y. Geng, J. Wang, S. Wu, H. Li, F. Yu, G. Yang, H. Gao and Z. Su, *J. Mater. Chem.*, 2011, **21**, 134–143.
87 M. Roknuzzaman, C. Zhang, K. Ostrikov, A. Du, H. Wang, L. Wang and T. Tesfamichael, *Sci. Rep.*, 2019, **9**, 718.
88 S. B. Aziz, M. A. Brza, M. M. Nofal, R. T. Abdulwahid, S. A. Hussen, A. M. Hussein and W. O. Karim, *Materials*, 2020, **13**, 3675.
89 M. Abdi-Jalebi, M. Ibrahim Dar, A. Sadhanala, E. M. J. Johansson and M. Pazoki, in *Characterization Techniques for Perovskite Solar Cell Materials*, Elsevier, 2020, pp. 49–79.
90 H. J. Joyce, J. L. Boland, C. L. Davies, S. A. Baig and M. B. Johnston, *Semicond. Sci. Technol.*, 2016, **31**, 103003.
91 X. D. He, K. E. Torrance, F. X. Sillion and D. P. Greenberg, *ACM SIGGRAPH Comput. Graph.*, 1991, vol. 25, pp. 175–186.
92 A. I. Kuznetsov, A. E. Miroshnichenko, M. L. Brongersma, Y. S. Kivshar and B. Luk'yanchuk, *Science*, 2016, **354**, aag2472.
93 M. Fox and G. F. Bertsch, *Am. J. Phys.*, 2002, **70**, 1269–1270.
94 T. Nagatomi, R. Shimizu and R. H. Ritchie, *Surf. Sci.*, 1999, **419**, 158–173.
95 M. Ben Gzaiel, I. Garoui, F. N. Almutairi, I. Mbarek and O. A, *Opt. Mater.*, 2024, **154**, 115664.
96 K. Sekar, L. Marasamy, S. Mayarambakam, H. Hawashin, M. Nour and J. Bouclé, *RSC Adv.*, 2023, **13**, 25483–25496.
97 T. Minemoto and M. Murata, *Sol. Energy Mater. Sol. Cells*, 2015, **133**, 8–14.
98 C. Walkons, R. Murshed and S. Bansal, *Sol. RRL*, 2020, **4**, 2000299.
99 *Next-generation 2D Nanomaterials for Sustainable Energy and Environment-oriented Applications: Electrocatalysis, Photoelectrocatalysis and Photocatalysis*, ed. N. Singh and A. Kumar, Royal Society of Chemistry, 2025.
100 M. M. Salah, M. Abouelatta, A. Shaker, K. M. Hassan and A. Saeed, *Semicond. Sci. Technol.*, 2019, **34**, 115009.
101 S. Tuo, K. B. M. K. Koffi, K. A. Kamenan, J. Datte and A. S. Yapi, *Model. Numer. Simul. Mater. Sci.*, 2024, **14**, 97–106.
102 J. D. Servaites, S. Yeganeh, T. J. Marks and M. A. Ratner, *Adv. Funct. Mater.*, 2010, **20**, 97–104.
103 O. K. Simya, A. Mahaboobbatcha and K. Balachander, *Superlattices Microstruct.*, 2015, **82**, 248–261.
104 Y. Li, B. Ding, Q.-Q. Chu, G.-J. Yang, M. Wang, C.-X. Li and C.-J. Li, *Sci. Rep.*, 2017, **7**, 46141.
105 A. D. Dhass, E. Natarajan and L. Ponnusamy, in *2012 International Conference on Emerging Trends in Electrical Engineering and Energy Management (ICETEEEM)*, IEEE, Chennai, Tamil Nadu, India, 2012, pp. 382–386.
106 X. Zhang, X. Chen, Y. Chen, N. A. Nadege Ouedraogo, J. Li, X. Bao, C. B. Han, Y. Shirai, Y. Zhang and H. Yan, *Nanoscale Adv.*, 2021, **3**, 6128–6137.

107 M. K. Hossain, M. K. A. Mohammed, R. Pandey, A. A. Arnab, M. H. K. Rubel, K. M. Hossain, M. H. Ali, Md. F. Rahman, H. Bencherif, J. Madan, Md. R. Islam, D. P. Samajdar and S. Bhattarai, *Energy Fuels*, 2023, **37**, 6078–6098.

108 J. Peng, Y. Wu, W. Ye, D. A. Jacobs, H. Shen, X. Fu, Y. Wan, T. Duong, N. Wu, C. Barugkin, H. T. Nguyen, D. Zhong, J. Li, T. Lu, Y. Liu, M. N. Lockrey, K. J. Weber, K. R. Catchpole and T. P. White, *Energy Environ. Sci.*, 2017, **10**, 1792–1800.

109 M. Jiang, Q. Niu, X. Tang, H. Zhang, H. Xu, W. Huang, J. Yao, B. Yan and R. Xia, *Polymers*, 2019, **11**, 147.

110 G. Lu, X. Wang, J. Du, M. Zhang, Y. Gao, Y. Liu, J. Ma and Z. Lin, *Coatings*, 2020, **10**, 46.

111 R. Yao, S. Ji, T. Zhou, C. Quan, W. Liu and X. Li, *Phys. Chem. Chem. Phys.*, 2024, **26**, 5253–5261.

112 B. Smith, Efficient lead-free perovskite solar cell, **https://443.ece.illinois.edu/files/2018/09/SolarCellReportSmithWaterMarked.pdf**, (accessed 10 May 2025).

113 S. Srivastava, A. K. Singh, P. Kumar and B. Pradhan, *J. Appl. Phys.*, 2022, **131**, 175001.

114 S. Bhattarai, R. Pandey, J. Madan, S. Tayeng, P. K. Kalita, M. Z. Ansari, L. Ben Farhat, M. Amami and M. K. Hossain, *RSC Adv.*, 2023, **13**, 26851–26860.

115 K. I. Ferdous Utsho, S. M. G. Mostafa, Md. Tarekuzzaman, M. S. M. Al-Saleem, N. I. Nahid, J. Y. Al-Humaidi, Md. Rasheduzzaman, M. M. Rahman and Md. Z. Hasan, *RSC Adv.*, 2025, **15**, 2184–2204.

116 M. K. Hossain, A. A. Arnab, R. C. Das, K. M. Hossain, M. H. K. Rubel, Md. F. Rahman, H. Bencherif, M. E. Emetere, M. K. A. Mohammed and R. Pandey, *RSC Adv.*, 2022, **12**, 34850–34873.

117 Y. He, L. Xu, C. Yang, X. Guo and S. Li, *Nanomaterials*, 2021, **11**, 2321.

118 M. S. Uddin, M. K. Hossain, M. B. Uddin, G. F. I. Toki, M. Ouladsmane, M. H. K. Rubel, D. I. Tishkevich, P. Sasikumar, R. Haldhar and R. Pandey, *Adv. Electron. Mater.*, 2024, **10**, 2300751.

119 Md. A. Bakkar Siddique, Md. S. Parves, Md. Tarekuzzaman, Md. R. Kabir, M. S. M. Al-Saleem, J. Y. Al-Humaidi, Md. Rasheduzzaman, M. M. Hossen, M. M. Rahman and Md. Z. Hasan, *Langmuir*, 2025, **41**(30), DOI: **10.1021/acs.langmuir.5c01639**.